JGR Solid Earth

RESEARCH ARTICLE
10.1029/2018JB017151

Characteristics of Ground Motion Generated by Wind Interaction With Trees, Structures, and Other Surface Obstacles

Christopher W. Johnson[1], Haoran Meng[2], Frank Vernon[1], and Yehuda Ben-Zion[2]

[1]Scripps Institution of Oceanography, University of California San Diego, San Diego, CA, USA, [2]Department of Earth Sciences, University of Southern California, Los Angeles, CA, USA

Key Points:

- Wind gusts above 2-m/s shaking surface objects produce earthquake- and tremor-like waveforms that vary spatially over tens of meters
- Wind-related ground motions exceed the PGV of *M*1.0–1.5 earthquakes for 6–31% of the day and inhibit detection of small earthquakes
- Recognition of wind-related signals can increase the performance of advanced algorithms for detecting small earthquakes and tremor

Correspondence to:
C. W. Johnson,
cwj004@ucsd.edu

Citation:
Johnson, C. W., Meng, H., Vernon, F., & Ben-Zion, Y. (2019). Characteristics of ground motion generated by wind interaction with trees, structures, and other surface obstacles. *Journal of Geophysical Research: Solid Earth*, *124*. https://doi.org/10.1029/2018JB017151

Received 7 DEC 2018
Accepted 13 JUL 2019
Accepted article online 18 JUL 2019

Abstract Analysis of continuous seismic waveforms from a temporary deployment at Sage Brush Flats on the San Jacinto fault reveals earthquake- and tremor-like signals generated by the interaction of wind with obstacles above the surface. Tremor-like waveforms are present at the site during wind velocities above 2 m/s, which occur for 70% of the deployment duration. The response to the wind has significant spatial variability with highest ground motions near large surface objects. The wind-related signals show ground velocities that exceed the average ground motions of *M*1.0–1.5 earthquakes for 6–31% of the day. Waveform spectra indicate a modulation of amplitude that correlates with wind velocity and distance from local structures. Earthquake-like signals are found to originate from local structures and vegetation, and are modified on length scales of tens of meters. Transient signals originating beyond the study area are also observed with amplitudes greater than some microseismic events. The wind-related ground motions contribute to local high-frequency seismic noise. Some of these signals may be associated with small failures of the subsurface material. During elevated wind conditions a borehole seismometer at a depth of 148 m shows increased energy in the 1–8-Hz band that is commonly used for earthquake and tremor detection. The wind-related earthquake- and tremor-like signals should be accounted for in earthquake detection algorithms due to the similar features in both time and frequency domains. Proper recognition of wind-related ground motions can contribute to understanding the composition of continuous seismic waveforms and characterize mechanical properties of the shallow crust.

Plain Language Summary Seismic recordings contain information on atmospheric and anthropogenic phenomena which can occur over much larger portions of the daily records than tectonic events. We characterize signals with earthquake- and tremor-like waveforms that are generated as wind gusts interact with objects on the surface and modulate the ambient environmental noise. The wind interaction may produce microfailures in the shallow crust generating high-frequency energy that contributes to the local seismic noise. The classification of nontectonic signals is becoming increasingly important as earthquake detection algorithms employ machine learning techniques that utilize the data to build a detection model. Properly identifying different classes of signals will provide better detection models as the algorithms continue to improve.

1. Introduction

Wind-related sources of ground motion are an important class of signals observed in continuous waveforms that can reduce the observation potential of seismic stations located in many environments and obscure tectonic events (De Angelis & Bodin, 2012; Lott et al., 2017; Naderyan et al., 2016; Withers et al., 1996). Daily and seasonal changes in atmosphere pressure and temperature produce ground motion at various frequency bands (Hillers & Ben-Zion, 2011; Sorrells, 1971; Sorrells et al., 1971; Sorrells & Goforth, 1973; Tanimoto & Wang, 2018) with increased noise amplitudes that correlate with the wind velocity produced by these atmospheric variations. Wind energy produces a wide variety of seismic signal that can vary over length scales of hundreds of meters and less (Dybing et al., 2019; Johnson et al., 2019). These signals are a superposition of horizontal and vertical motions from long-wavelength atmospheric pressure waves (Sorrells et al., 1971), shear stress perturbations induced by near-surface wind-induced turbulence (Naderyan et al., 2016; Raspet et al., 2008; Yu et al., 2011), direct interaction of wind with the sensor or in situ surface structures (Dybing et al., 2019; Johnson et al., 2019; Mucciarelli et al., 2005; Withers et al., 1996), and possibly local subsurface

failures generated by these effects. Establishing the source, duration, and characteristics of wind-related energy in seismic records is essential to developing correct interpretations of these regularly occurring phenomena and improving the detection of tectonic seismic signals.

Wind-generated ground motions may cover a large portion of the day with waveform amplitudes similar to or larger than those produced by microseismicity ($M < 2$; Withers et al., 1996) and tectonic tremor. A pressure power spectral density (PSD) of 10 Pa^2/s is found to be a lower threshold to produce vertical ground motions at frequencies in the 0.01–0.02-Hz band that can exceed other sources of seismic noise (Tanimoto & Valovcin, 2016). Above this pressure threshold the variations in long-period seismic noise represent vertical displacements and horizontal tilts that provide constraints on subsurface elastic properties (Tanimoto & Wang, 2018). The ground motions produce a systematic increase in the lower limit of the PSD for wind speeds greater than 3 m/s, thereby reducing the detection threshold for other geophysical signals of interest. Proper recognition of wind-related ground motions can contribute to understanding the composition of continuous seismic waveforms and characterize mechanical properties of the shallow crust through variations in noise levels in different environments.

The increase in the number of seismometers at regional and local scales provides opportunities for detecting, locating, and analyzing weak seismic signals from tectonic and other sources. The use of easy-to-deploy, low-cost, autonomous geophones that produce high-quality seismic recordings are providing detailed data sets for identifying and characterizing new signals. Dense seismic arrays typically operate for a short duration (e.g., less than 35 days) with increased spatial resolution (e.g., tens to hundreds of meter spacing) and a high sample rate (e.g., 250–1,000 Hz) that facilitate investigating weak coherent signals propagating in the shallow crust. Spatially dense arrays can be used for detection and analysis of sources that have a signal-to-noise ratio (SNR) close to and below 1, allowing for the identification of earthquakes, tremors, or other signals that are buried in the noise (e.g., Ben-Zion et al., 2015; Ross et al., 2017; Schmandt & Clayton, 2013; Shelly et al., 2016). Advances in techniques for detecting small earthquakes and tremor (Aguiar & Beroza, 2014; Barrett & Beroza, 2014; Hammer et al., 2012; Meng & Ben-Zion, 2018b; Perol et al., 2018; Reynen & Audet, 2017; Ross et al., 2018; Yoon et al., 2015) increase the need to properly decipher nontectonic transient signals in the waveforms that are originating at the surface from anthropogenic and other natural phenomenon (e.g., Inbal et al., 2018; Meng & Ben-Zion, 2018a; Riahi & Gerstoft, 2015). Extracting the correct information from seismic waveforms requires a clear understanding of local and regional anthropogenic sources, and the coupling of atmospheric processes with the solid Earth to properly identify differences between tectonic and nontectonic signals.

Correct labeling of wind-related events and other sources of ground motion will greatly increase the ability to detect microseismicity and track tectonic deformation at depths. Quantifying the total daily fraction that seismic records contain atmospheric-related signals will decrease false detections of other phenomenon. An improved ability to detect and classify sources producing ongoing ground motion is also important for tomographic imaging based on the ambient seismic noise, which requires a diffuse wavefield and the removal of all localized sources (e.g., Bensen et al., 2007). Fully diffuse noise requires a stationary wavefield with uncorrelated wave modes at different frequencies (Liu & Ben-Zion, 2016; Sánchez-Sesma et al., 2008; Weaver, 1982) and is fundamental for deriving accurate Green's functions from cross correlations of ambient seismic noise (e.g., Campillo et al., 2011; Lobkis & Weaver, 2001). Defining the characteristics of different classes of waveforms for earthquakes, wind, air-traffic, trains, cars, and other sources of ground motion will advance the utility of dense arrays and regional seismic networks. The main objective of this paper is to define characteristics of wind-related ground motion in dense array data.

The Sage Brush Flat (SGB) site on the San Jacinto Fault Zone (SJFZ) southeast of Anza, California is the location of a previous dense geophone deployment (Ben-Zion et al., 2015) and various studies associated with detailed imaging of the subsurface material (Hillers et al., 2016; Mordret et al., 2019; Roux et al., 2016) and detection of small earthquakes and air-traffic events (Meng & Ben-Zion, 2018a, 2018b). Using a frequency-domain matched-field processing technique involving beamforming and backprojection of continuous array data (Corciulo et al., 2012; Kuperman & Turek, 1997), very small events were detected at the SGB site and were found to cluster near structures, fences, and within the vegetation. The locations suggest that these events are associated with shallow ground motion generated at the foundations of these objects by wind gusts (Gradon et al., 2019). In the present study we attempt to

clarify properties of ground motion generated by trees, structures, and other surface objects that are shaken by the wind. The study employs data from a temporary nodal array deployed for one month at the SGB site. The data are a mixture of wind-generated ground motions, earthquakes, air traffic, and additional unidentified sources of emergent and impulsive noise signals. The seismic records are augmented by meteorological measurements to quantify the wind velocity in relation to time intervals containing earthquake-like and tremor-like signals. Detailed waveform analyses in time and frequency domains are used to characterize all periods of elevated wind velocity and the coupling of the structures to the ground. We evaluate the total fraction of a day that contains wind-related signals and quantify the change in noise amplitude during the wind events. The results indicate that tremor-like signals occur when the wind velocity is above 2 m/s. Wind-related ground motions at the SGB site are found to exceed the expected ground velocity of local M1.0–1.5 events for 6–31% of the day.

2. Sage Brush Flat Study Area, Data, and Methods

The analysis is based on continuous seismograms recorded for a one-month period in a ~0.1-km^2 area at SGB atop the damage zone of the Clark branch of the SJFZ southeast of Anza, California. The site is a local fault zone valley that has variable wind levels throughout the day and is the same location of the dense nodal array deployed in 2014 (Ben-Zion et al., 2015). The location is privately owned and contains structures, unused machinery and equipment, an unused airstrip, some fencing, and natural trees and brush. We deployed 40 three-component 5-Hz Fairfield ZLand seismometers, referred to as nodes, from 9 February to 17 March 2018 and obtained continuous ground velocity measurements at 500 Hz with 12-dB gain. The nodes were arranged in a configuration to target in situ structures with a nominal station spacing of 30 m in a 350 × 300-m area (Figure 1).

In the eastern extent of the study area 11 nodes were deployed parallel to the fault along the fencing and in the natural vegetation (group 01 in Figure 1). To the north 17 nodes were aligned in cardinal directions around an open-air covered parking structure with 1 in the center and 4 extending in each direction (group 02 in Figure 1). In the southern section of the site 12 nodes were deployed around a housing structure with 3 in each cardinal direction (group 03 in Figure 1). The nodes were secured to the ground with a spike mount, oriented to the north, and leveled; no attempt was made to bury the sensors, which can reduce noise levels in the horizontal component by ~15 dB but negligible gains are observed in the vertical channel (Sweet et al., 2018). Located on the property is the Plate Boundary Observatory borehole seismometer B946 installed at a depth of 148 m and in continuous operation since 2010 recording at 100 Hz (yellow square in Figure 1). The relatively quiet borehole seismometer is used in conjunction with the nodes to identify surface generated signals that are observable at depth. The seismic instrument response is removed by detrending the daily traces, applying a cosine taper, and deconvolving the sensitivity and response sensor transfer function to obtain ground motion in units of m/s.

The wind velocity was recorded as 1-min average and maximum values using an anemometer installed about 3.5 m above the ground and located approximately 20 m southeast of the covered parking structure (Figure 2). The average wind velocity during the deployment is 1.9 m/s with maximum wind gust reaching 14.9 m/s. The wind direction is nearly constant between 315° and 345° following the topography of fault zone ridges and blowing generally from northwest to southeast. Each day is examined for the total duration of wind velocity in 1-m/s intervals and shown as the daily percentage. A wind velocity of 2–3 m/s is recorded for ~30% of each day during the experiment.

The spectral analysis is performed using an adaptive weighted multitaper method with a time bandwidth product of four and seven discrete prolate spheroidal sequences (Prieto et al., 2009; Thomson, 1982). Spectrograms are produced using a 1-s interval for short durations and a 60-s interval for daily records, both with a 95% overlap and zero padded to the next power of 2. The PSD units are in decibel (dB) as 10 $\log_{10}$ ($m^2 \cdot s^2 \cdot Hz$). Additionally, the seismic data are analyzed in 60-s nonoverlapping intervals to produce spectra from 0 to 250 Hz. The wind data provide a quantitative metric to group each spectrum by the reported wind velocity using a 1-m/s interval from 0 to 4 m/s. The median spectra are calculated for the PSD estimate for each node as a function of the average wind velocity.

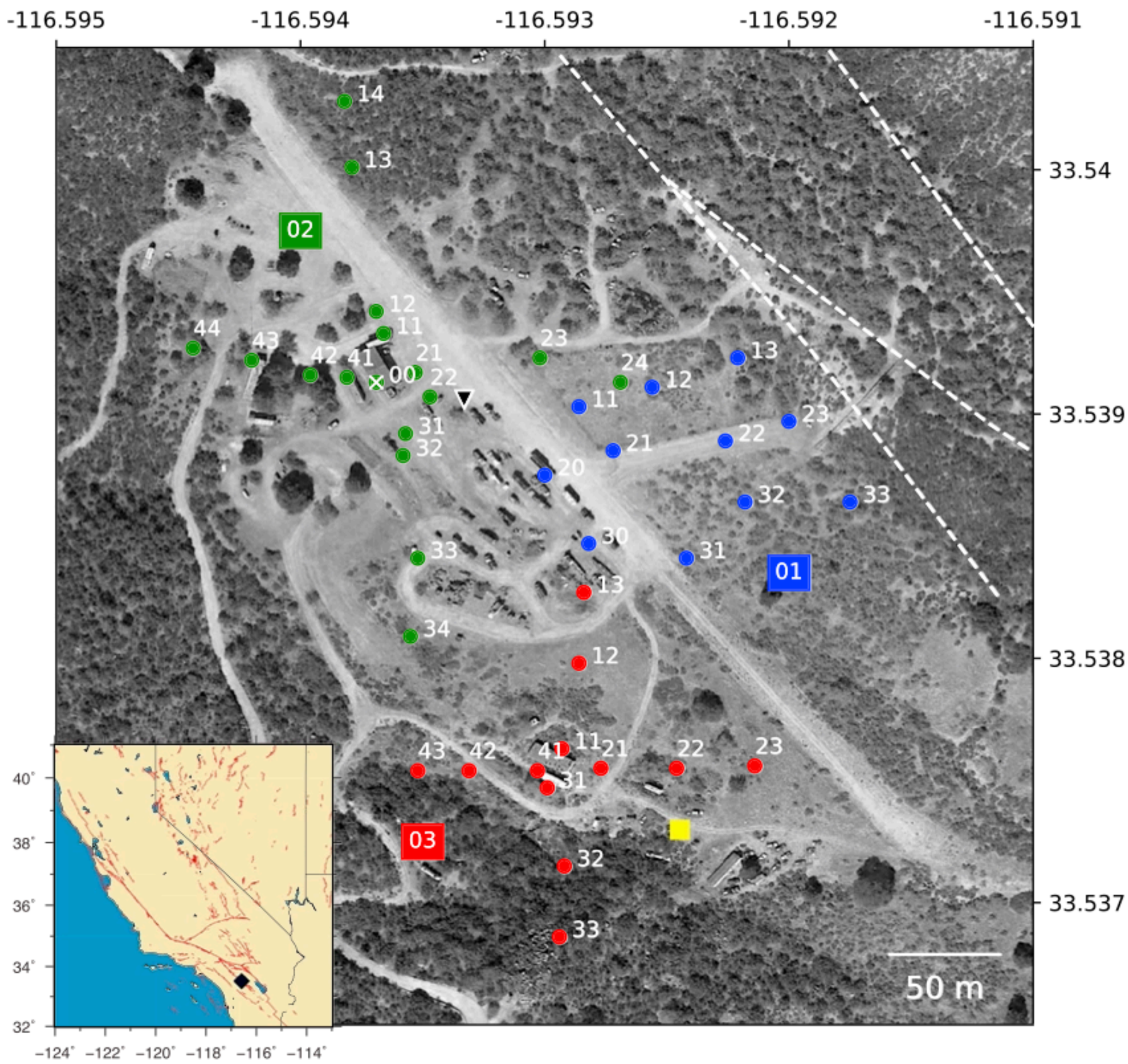

Figure 1. Node deployment locations on GoogleEarth image with inset map showing the location on the San Jacinto Fault. The nodes are arranged around the vegetation (group 01 in blue), the covered parking structure (group 02 in green), and a housing structure (group 03 in red). The anemometer location is marked by the inverted black triangle near the center of group 02. The permanent borehole seismometer B946 is shown as the yellow square southeast of group 03. The dashed white lines are mapped USGS fault traces.

3. Wind-Generated Ground Motions

3.1. Peak Ground Velocity From Wind Shaking Surface Objects

To quantify the spatial variability of peak ground velocity with wind velocity we calculate the average peak ground velocity (PGV) for 300-s moving windows with a 60-s overlap using unfiltered seismic data collected between day of year (DOY) 50–60. The moving average PGV is compared to the 60-s average wind velocity and shows a log linear correlation for both the horizontal and vertical ground motions for a single node 01-32, with 01 denoting the group and 32 the sensor, located around the vegetation (Figure 3a). In all wind conditions the horizontal ground motion exceeds the vertical and a day of week dependence is not observed. The linear fit to the wind velocity and PGV is calculated using robust L1 regression to suppress PGV outliers. The slope of the fitted curve represents the expected noise produced by wind generated ground motions in response to in situ objects shaking in the wind and the intercept is the noise amplitude without wind (Figure 3b). The data for node 01-32 have a slope of $10^{0.37}$ (m/s) per wind velocity (m/s) for horizontal ground motions with an intercept of $10^{-5.3}$ (m/s). The vertical is $10^{0.21}$ (m/s) per wind velocity (m/s) with an intercept of $10^{-5.6}$ (m/s).

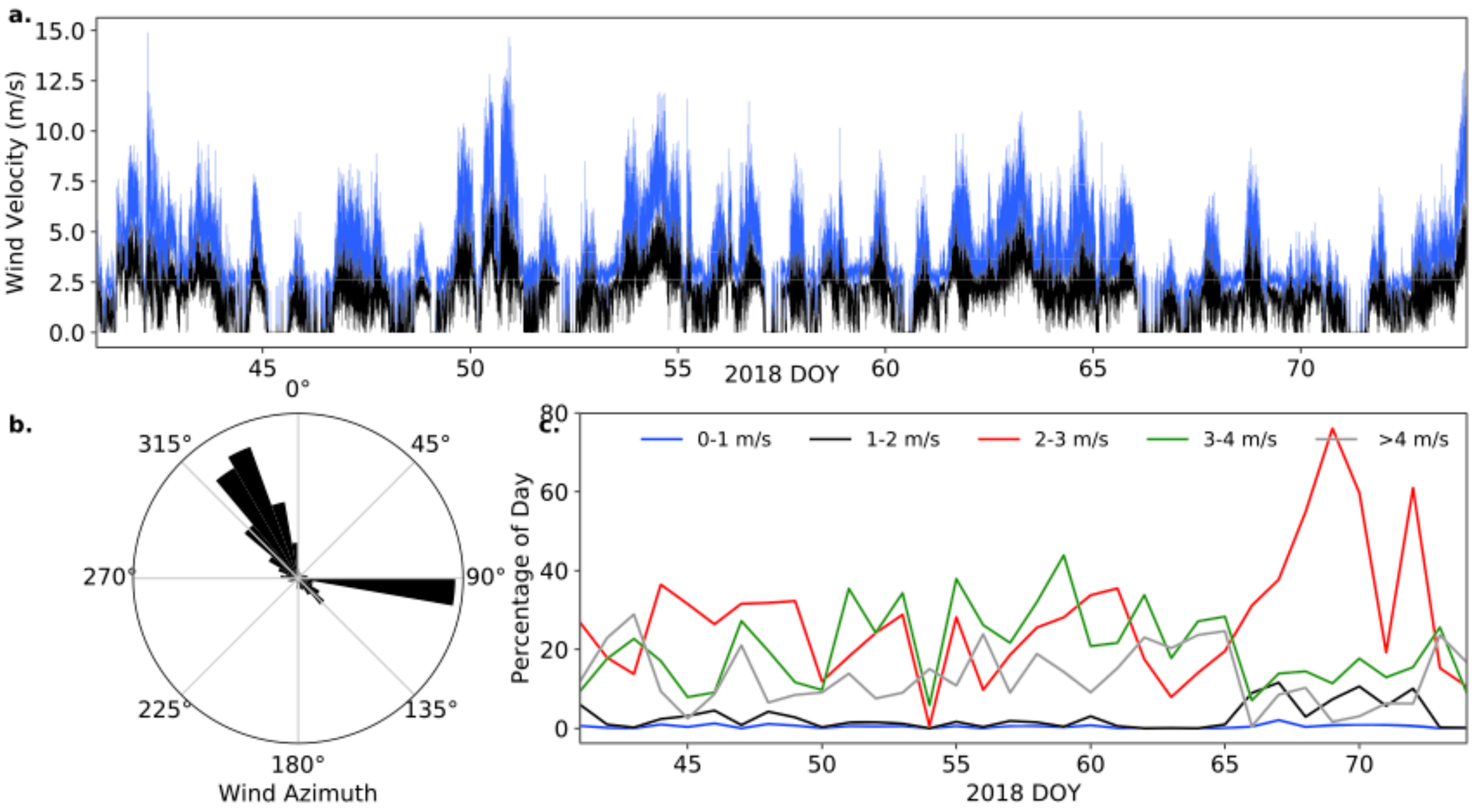

Figure 2. (a) Wind velocity during the nodal deployment. The velocity is reported as 1-min averages (black) with maximal wind gusts during the same intervals (blue); the maximum recorded wind gust is 14.9 m/s. (b) Histogram of the wind azimuth showing an orientation subparallel to fault generally going from northwest to southeast. (c) The percentage of each day when wind conditions are within 1-m/s intervals.

Extending this analysis to all stations shows significant spatial variability of the ground response to wind with the largest values at nodes located in close proximity to large surface objects (Figure 3c). Throughout the study area the horizontal ground response to wind is greater than the vertical. The highest values are at a node located near a covered parking structure with a distance dependence observed in the neighboring nodes. A node located among unused machinery also shows similarly high values. The nodes located near trees and bushes show higher amplitudes near the fence (node group 01 sensors 22 and 33). The nodes farthest north are among tress and show similar response to those in the bushes. The nodes to the southwest on the hillslope show minimal response in both horizontal and vertical ground motion and are juxtaposed by the southernmost node situated atop the hill and more exposed to the wind. The correlation between ground shaking and proximity to surface objects suggest that the signals are not dominated by wind interacting directly with the nodes but generated by a combination of multiple sources.

The spatial distribution of seismic noise amplitude during minimal wind is shown as the fitted curve intercepts (Figure 4). The pattern reveals noisy and quiet node locations with areas near trees and bushes having background noise amplitudes similar to those near machinery. The minimum horizontal and vertical seismic noise velocities are $10^{-5.5}$ and $10^{-5.7}$ m/s, respectively. None of the vertical ground velocities are greater than the horizontal. Aggregating the PGV for the average and peak wind velocity intervals using all nodes between DOY 50 and 60 further confirms a log linear relationship between PGV and wind gust velocity (Lott et al., 2017), with horizontal ground motions exceeding the vertical (Figure 5). The interval containing 90% of the PGV values for each wind velocity interval shows a change point where the PGV increases above 1–2 m/s. The horizontal velocity indicates increasing seismic noise above $10^{-5.5}$ m/s during wind conditions >1 m/s. The vertical shows a similar response but wind velocity over 2 m/s is needed to increase above $10^{-5.5}$ m/s. Wind gust velocities >3 m/s are observed for 70% of the 33-day deployment, suggesting that a portion of other weak signals are masked during the elevated wind conditions. We find that 6.0 ± 4.2% of the daily waveforms contain amplitudes above the upper 90% interval of $10^{-4.5}$-m/s ground motion during wind velocities ≥2 m/s (Figure 5). Applying the same metrics to the horizontal seismic velocity, the percentage increase to 31.3 ± 16.3% of the day.

The quietest location is on the southwest hill slope and the noisiest is east of the covered parking structure (Figure 3). The energy originating from the covered parking structure shows values decreasing in all

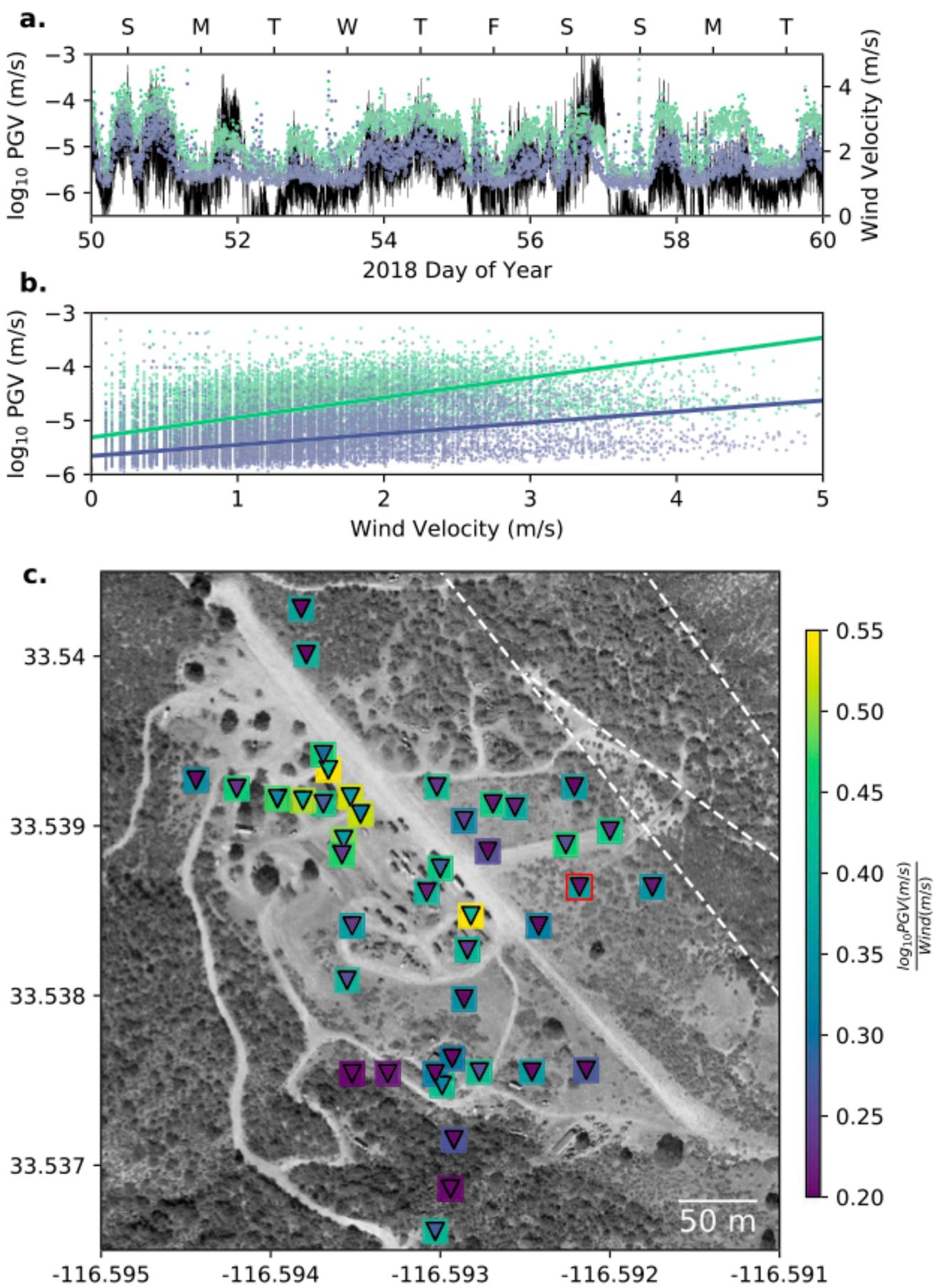

Figure 3. Peak ground velocity (PGV) response to the wind. (a) Data for node in group 01 sensor 32 showing moving average PGV for the horizontal (green) and vertical (blue) ground motions for 10 days during the deployment. The 60-s average wind velocity is shown in black. The top axis indicates the day of week by a single letter. (b) Robust linear regression curve for wind velocity versus PGV for horizontal and vertical ground motions. The slope of the horizontal curve is $10^{0.37}$ (m/s) per wind (m/s) and the vertical curve is $10^{0.21}$ (m/s) per wind (m/s). (c) Slope of the robust regression for all nodes in map view for the horizontal (square symbols) and vertical (inverted triangle in square) motions. The node outlined in red is represents the data shown in (a) and (b).

directions and is explored further by comparing the PSD as a function of distance and wind velocity. The PSD for the five nodes extending 128 m north from the covered parking structure is shown in Figure 6 for the north-south and vertical ground motions. The PSD is calculated using the entire 35-day deployment for every 1 min of nonoverlapping seismic data and grouped by the 1-min average wind velocity. The median of the spectra for each 1-min wind velocity interval exhibits a variety of features that vary over the 128-m distance, notably a systematic increase with the wind velocity and a decrease with distance from the parking structure. All nodes show higher PSD values in the horizontal than the vertical, which is consistent with the PGV values in Figure 3. The maximum PSD is observed during the 3–4-m/s wind velocity at node 02-11 and shows a reduction of 5 dB per 1-m/s decrease in wind velocity across the entire spectral bandwidth. Nodes 02-00 and 02-11 show similar features and are situated on opposite sides of the

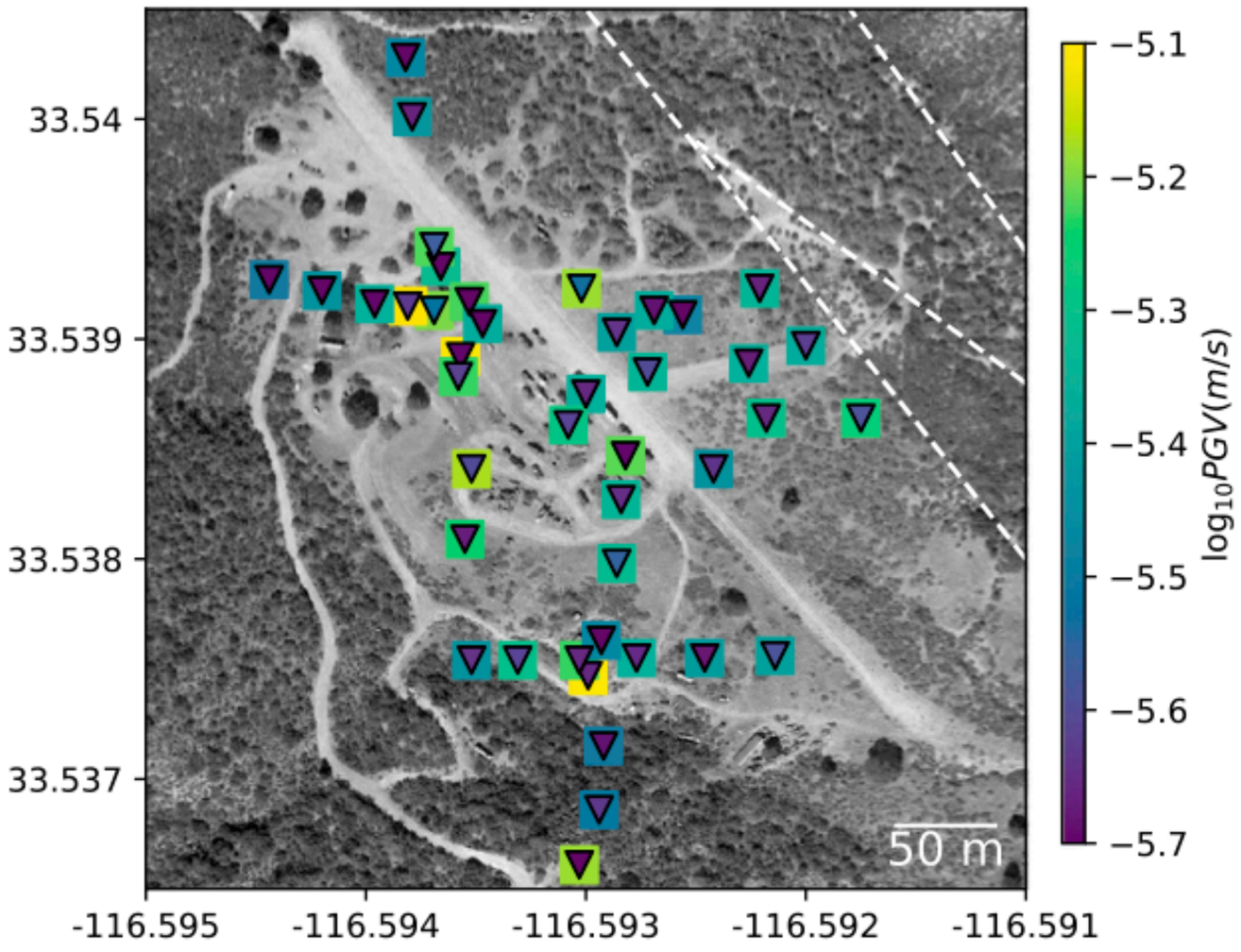

Figure 4. PGV values during no wind conditions for horizontal (square) and vertical (inverted triangle) motions based on the curve fit intercepts in Figure 3.

parking structure and storage unit. A 20-dB decrease is observed at node 02-14 to 02-11 during the 3–4-m/s wind velocity with a reduction of about 5 dB between wind velocity intervals at both locations. The results indicate that a local structure is coupling wind energy to the shallow surface (Naderyan et al., 2016), which can propagate at least 128 m from the source and modify the instrumental noise across a broad range of frequencies.

In each spectrum shown in Figure 6 a peak is observed between 35 and 50 Hz, regardless of wind velocity, that shifts to higher frequencies as the distance from the covered parking structure increases. The spectra for node 02-13 contain two peaks centered near 50 Hz that shift to higher frequencies with increased velocity. A similar pattern is observed at node 02-14 for the 3–4-m/s wind velocity. Johnson et al. (2019) and Farrell et al. (2018) performed detailed analyses exploring this 40-Hz signal and found a frequency modulation for this peak amplitude as a function of wind and temperature changes that is unique to these instruments. The spectral content of the signal changes under multiple conditions when the instruments are installed on the surface or buried, and shows the greatest frequency modulation when temperatures drop below 0 °C, suggesting that it is a function of ground coupling. One explanation for the increased amplitude is that a combination of nearby structures and trees coupling wind energy in to the ground induce nonlinear response at the shallow subsurface and excite different resonance frequencies (Johnson et al., 2019). This feature of the data should be considered when examining high-frequency (>30 Hz) signals.

Wind-generated ground motions can reduce the ability to detect small earthquakes, even with borehole instruments at 85-m depth (Withers et al., 1996). The borehole seismometer B946 shows evidence for wind-generated ground motions observable at a depth of 148 m (Figure 7). Contrary to the nodes deployed to target local structures as possible sources of noise, the borehole seismometer was installed at depth to isolate the sensor from surface-generated noise. The proximity of the borehole seismometer to sources of wind-generated ground motions in this study provides a good test case for the noise variations as a function of wind velocity. The spectrograms from DOY 50–60 reveal an increase of power in the 1–8-Hz band for the vertical and horizontal seismic signals during sustained wind velocity above 2 m/s (Figures 7c and 7e). A close-up of the waveforms indicates an undulation of the noise as a function of wind velocity that correlates with increased power up to 8 Hz. The source of noise is not suspected to be anthropogenic since the signal is present during nighttime hours and diminishes during periods of lower wind velocity. However, it is in the same frequency band for noise associated with wind turbines, train and vehicle traffic, and other sources of cultural

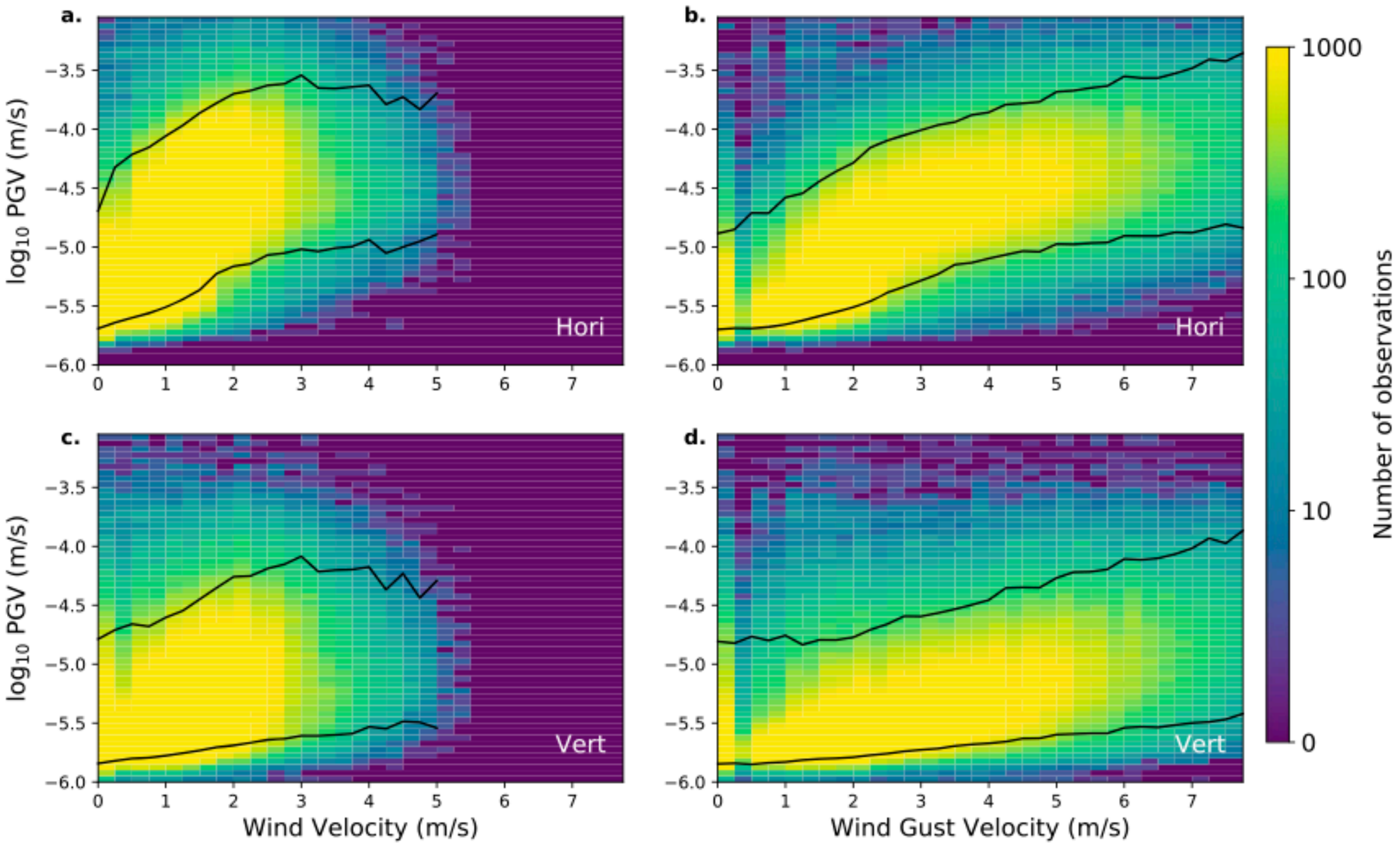

Figure 5. Peak ground velocity (PGV) versus wind velocity shown as a 2-D histogram for all nodes in the study area for data between DOY 50 and 60 for (a) the horizontal velocity and 1-min average wind velocity, (b) the horizontal velocity and 1-min peak gust wind velocity, (c) the vertical velocity and 1-min average wind velocity, and (d) the vertical velocity and 1-min peak gust wind velocity. The black lines show the interval containing 90% of the PGV values for each wind velocity interval.

noise in this region, which could contribute to some of the amplitude increase (Inbal et al., 2018; Marcillo & Carmichael, 2018). A plausible explanation is that these signals may be associated with numerous small failures of the subsurface material that is strained by the wind loading of the surface objects. The weak shallow material under low confining stress would be prone to local failures producing bursts of high-frequency waves (e.g., Ben-Zion & Ampuero, 2009). The very low attenuation coefficient of the shallow material (e.g., Aster & Shearer, 1991; Liu et al., 2015) precludes propagation of high-frequency waves over large distances and implies that such data are generated locally. The increase in power occurs in the bandwidth ideal for monitoring earthquakes, effectively reducing the detectability of microseismic events or tremor even in borehole seismometers. This observation from a remote location at depth suggests that seismic data recorded at shallow depth contain wind-generated noise (e.g., Dybing et al., 2019; Withers et al., 1996) with earthquake- and tremor-like features, and require additional scrutiny for detections of weak earthquakes and tectonic tremor signals.

Ground motions from earthquakes are expected to scale as a function of magnitude, distance from source to receiver, and other source parameters such as stress drops and rupture velocity (Kwiatek & Ben-Zion, 2016). Around the SJFZ, the average horizontal PGV generated by local earthquakes at near-zero epicentral distance is $10^{-4.4}$ m/s for M1.5–2.0 events, $10^{-3.8}$ m/s for M2.0–3.0 events, and $10^{-2.8}$ m/s for M3.0–5.0 events, and the data indicate the PGV can vary by multiple orders of magnitude (Kurzon et al., 2014). We calculate PGV estimates for the SGB study area using the vertical channel of the nodes for 345 M1.0–3.4 local earthquakes occurring within 150 km of the array. The arrival times are selected using the P wave arrival picked from the borehole seismometer B946 to avoid estimating travel times. The events grouped into magnitude ranges of M1.0–1.5, M1.5–2.0, and M2.0–3.4 and shown with the SNR as a function of distance (Figure 8).

The results indicate vertical PGV values ranging from $10^{--3.0}$ to $10^{-6.5}$ m/s for all the events. For the population of events between M1.0 and 1.5 the SNR is below 2 for 11% of the events and a range of values between $10^{-4.0}$ and $10^{-6.5}$ m/s is observed. The events between M1.5 and 2.0 contain only 3% with an SNR below 2 and show a similar range of values. The population of the largest magnitude events between M2.0 and 3.4 have <1% of the observations with SNR below 2. This analysis is repeated for the north and east seismic

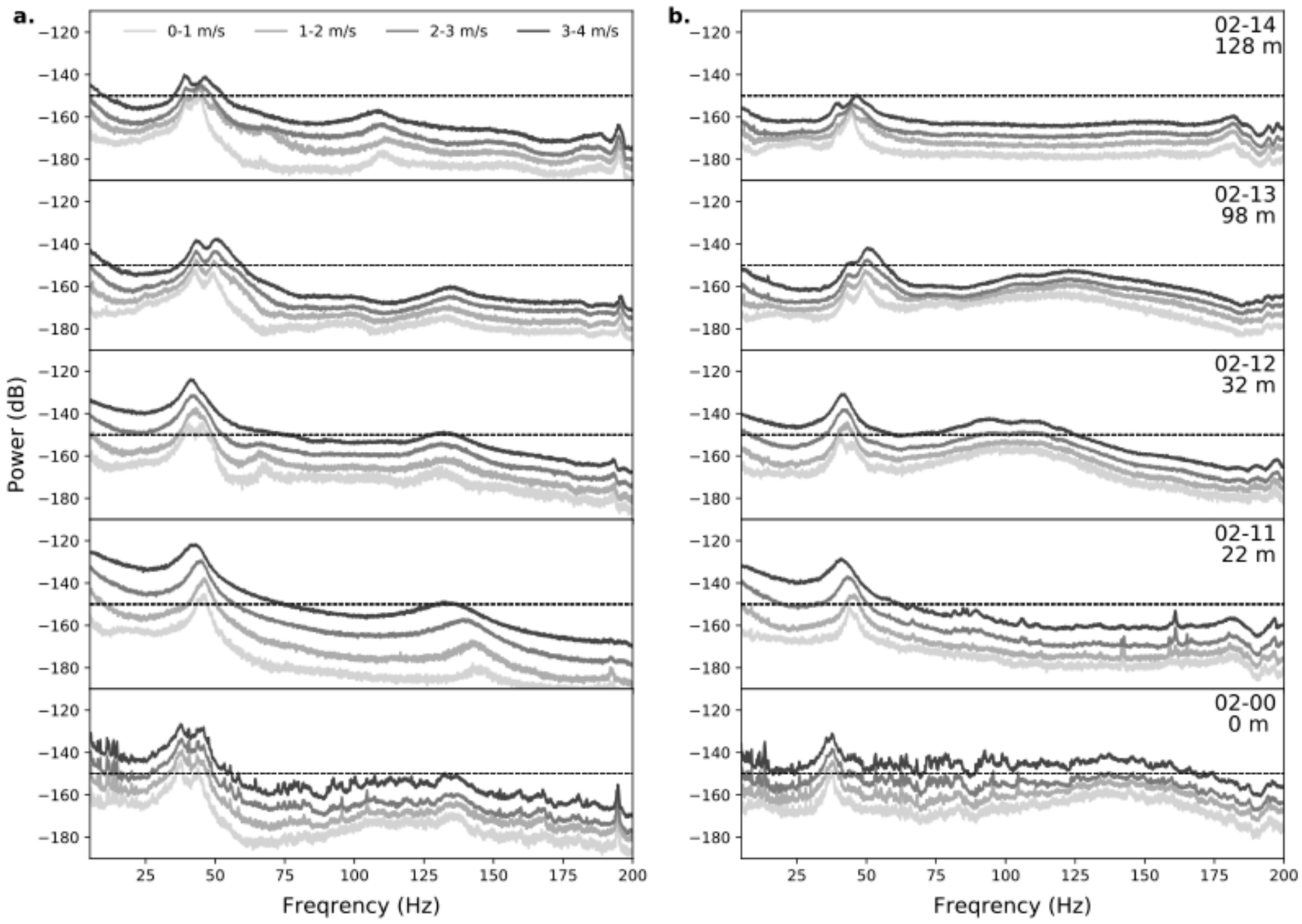

Figure 6. Spectra for the (a) north and (b) vertical seismic data as a function of distance from the covered parking structure and wind velocity for nodes in group 02 deployed along the northern transect (00, 11, 12, 13, 14). For each 1-min waveform, the spectrum is calculated and the median value is shown for each average wind velocity interval. The node label and distance in meters from the parking structure are shown in each panel in (b) and the color denotes the wind velocity interval.

channels and similar percentages are obtained. Using the seismic noise velocity of $10^{-5.5}$ m/s during low conditions (Figure 5) we estimate 55% of M1.0–1.5 earthquakes during the deployment have recorded PGV below this threshold. For the M1.5–2.0 and M2.0–3.4 population of events the percentages are 38% and 25%, respectively. Without access to the borehole seismometer to pick the exact arrival times the nodes would have reduced observation potential during elevated wind conditions especially if installed in or near a built structure (Dybing et al., 2019; Johnson et al., 2019; Naderyan et al., 2016). The percentages presented should be considered a lower bound for tectonic tremor observations, which we expect to be more obscured than small earthquakes during elevated wind conditions due to the characteristics of tremor and wind being similar (Inbal et al., 2018).

3.2. Earthquake- and Tremor-Like Signals Generated by the Wind

The daily continuous waveforms from node 01-33, located near the fence adjacent to the fault (Figure 1), show earthquake- and tremor-like waveforms that correlate with the changing wind velocity (Figure 9). The waveforms are band-pass filtered from 5 to 20 Hz to show representative ground motions in the frequency band typically used for earthquake monitoring. The node is surrounded by vegetation and is ~30 m from the fence, ~175 m from the housing structure, and ~200 m from the covered parking (Figure 1). The tremor-like waveforms are most apparent when the wind gust velocity is >2 m/s. Inspection of short time windows within the multihour tremor-like signal reveals earthquake-like waveforms with an impulsive arrival followed by higher amplitudes with a duration less than 10 s (Figures 9b and 9c). The waveforms exhibit characteristics similar to tectonic earthquakes with an impulsive arrival similar to a P wave followed by longer-period ground motion similar to a S wave on all seismic channels for both examples. The spectrogram for the vertical waveform shown in Figure 3c contains high-frequency energy during the earthquake-like signal with a pronounced increase around 40 Hz that is not observed at the neighboring node located 30 m to the west (Figure 10). One noticeable difference from a tectonic earthquake is the

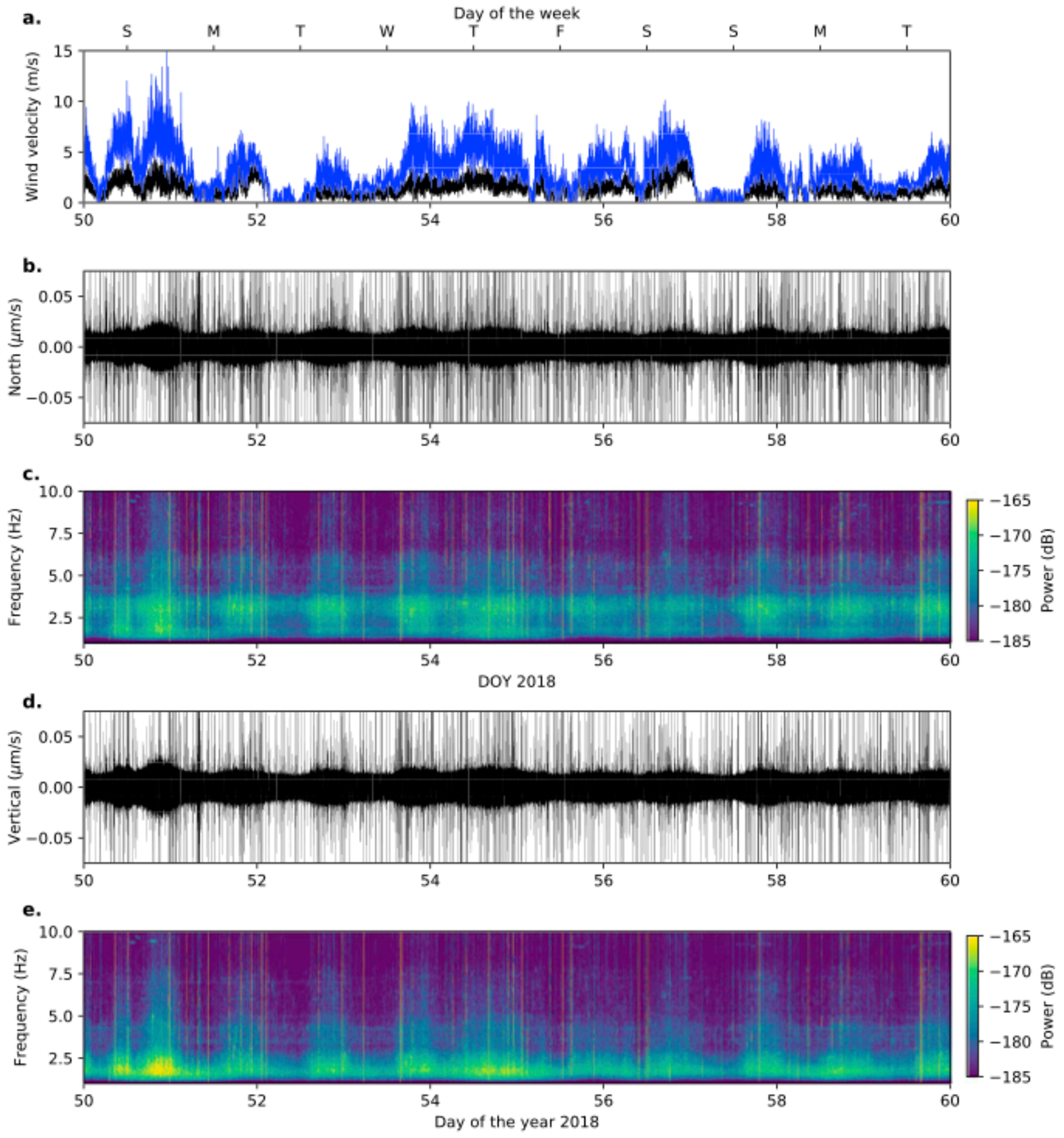

Figure 7. Wind velocity, seismic waveforms, and spectrogram for borehole seismometer B946 at 148-m depth for day of year 50–60. (a) Wind velocity is shown as the 1-min average in black and the 1-min peak in blue. The top axis shows the day of the week by letter. (b) North seismic channel with the vertical axis limited to ±0.05 μm/s and (c) the corresponding spectrogram limited to 0–10 Hz. (d) The vertical seismic channel and (e) corresponding spectrogram with the same axis limits.

lack of high-frequency energy during the *P* wave-like first arrival. Instead, the power in the signal is concentrated 3 s later in the wave packet during the later arrivals. This is a possible distinguishing feature between the wind-generated earthquake-like waveforms and tectonic events when applying microseismic detection techniques.

The earthquake- and tremor-like waveforms shown in Figures 9 and 10 are not unique to the day or node selected. Similar waveform characteristics are observed in all nodes in the study area throughout the duration of the deployment. The examples presented are impulsive waveforms, but many have a weak emergent arrival followed by an earthquake-like waveform. Interestingly, the earthquake-like waveforms are not always observable at adjacent nodes so the signals are modified considerably during propagation even over short distances. This is seen in the waveforms and spectrograms in Figure 10 for two nodes located about 30 m apart, with one containing an earthquake-like waveform with increased energy up to 50 Hz and the other showing little change. These examples demonstrate the variability in the earthquake-like waveforms and the need to carefully classify these signals at different locations. The lack of a coherent signal within 30 m suggests that signals are generated in close proximity to a node but attenuate quickly in the subsurface where the *Q* values are as low as 10 (Aster & Shearer, 1991; Liu et al., 2015). Assuming a shallow crustal velocity of 400 m/s and node spacing of 30 m, the amplitude is expected to decay by a factor of 0.8 and 0.3 for

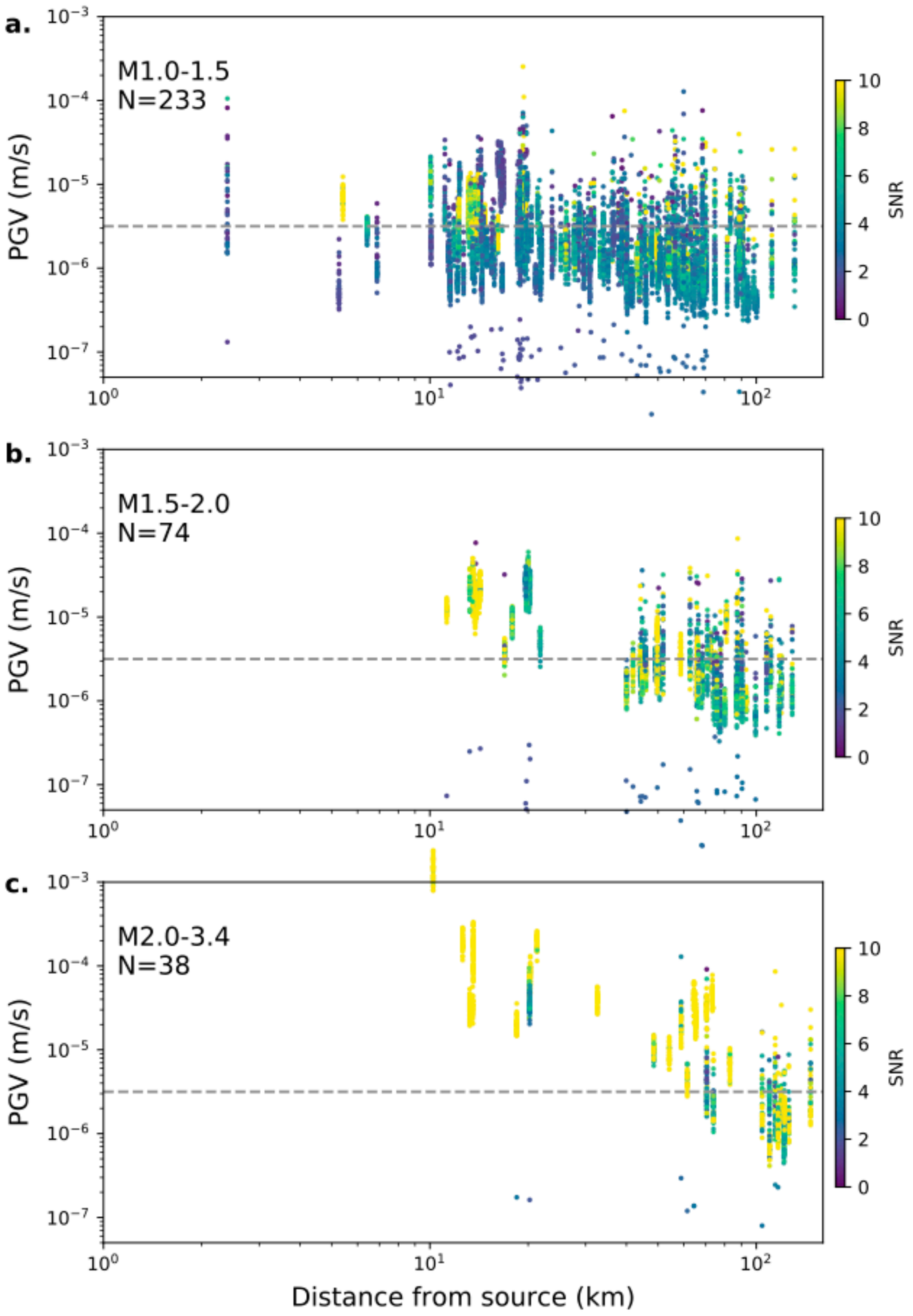

Figure 8. Vertical component peak ground velocity (PGV) for 345 M1.0–M3.4 earthquakes within 175 km of the nodal deployment. PGV is shown as a function of distance from the earthquake origin for (a) 233 M1.0–1.0 events, (b) 74 M1.5–2.0 events, and (c) 38 M2.0–3.4 events. The color of each indicates the signal-to-noise ratio (SNR), which saturates at 10, and the horizontal dashed line is $10^{-5.5}$ m/s.

waves at 10 and 50 Hz, respectively. The damaged fault zone material in the top 50 m can have S wave velocity of 200 m/s (e.g., Bonilla et al., 2002; Zigone et al., 2019), which decreases the values to 0.6 and 0.1 for waves at 10 and 50 Hz, respectively. A second important consideration is a similar degree of coupling at the specific node to observe comparable signals over short distances. We assume that the installation is sufficient to provide usable data and did not further test coupling effects. The sources for the earthquake- and tremor-like waveforms are likely superposition of signals generated by nearby buildings, machines, trees, and brushes that shake during the wind gusts and are coupled to the ground to produce broad spectrum signals.

The waveforms from node 02-11 are representative of a sensor that is installed near a built structure and susceptible to increased noise from the foundations during wind gusts, while node 02-14 is located to the north

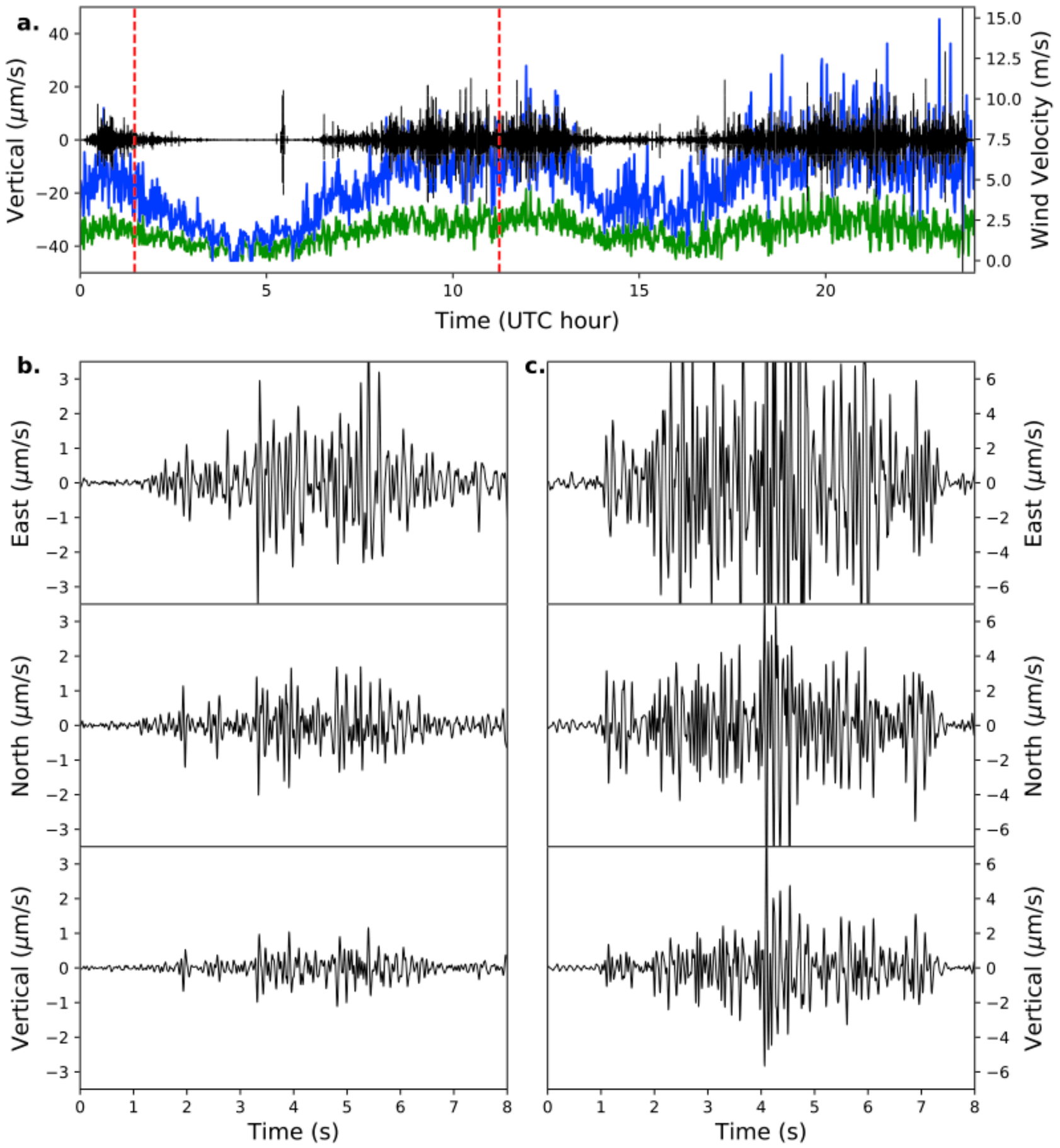

Figure 9. (a) Daily trace of vertical velocity for node 01-33 during DOY 50 shown with the 1-min average wind velocity (green) and maximum wind velocity (blue) to display the tremor-like signals produced by wind interacting with the vegetation. The seismic waveforms are filtered between 5 and 20 Hz to show the representative ground motions in the frequency band typically used for earthquake monitoring. The red lines correspond to the time of the east, north, and vertical waveforms shown at (b) 19 February 2018 01:27:46 UTC and (c) 19 February 2018 11:14:48 UTC which exhibit earthquake-like waveforms within the tremor-like signals.

in the trees (Figure 1). The data from node 02-11 contain the highest PGV increase during wind changes due to the proximity to the nearby covered parking structure, while data from node 02-14 are closer to the average (Figure 3). To show characteristics of the waveforms from the same node during different wind conditions, we select DOY 46 and 50 to represent days with low and high wind velocity, respectively. On DOY 46 there is an extended period of wind velocity <1 m/s, and on DOY 50 there are two periods where the average wind velocity is up to 3 m/s with wind gusts >14 m/s.

The vertical waveforms for node 02-11 are shown for 10-11 UTC during nighttime hours (2–3 am local time) to reduce anthropogenic sources of ground motion for low and high wind velocity conditions (Figure 11). Four low-amplitude infrequent bursts in the waveforms are observed when the wind velocity is below 1 m/s. These bursts in the waveforms are not associated with four *P* wave arrivals from small earthquakes

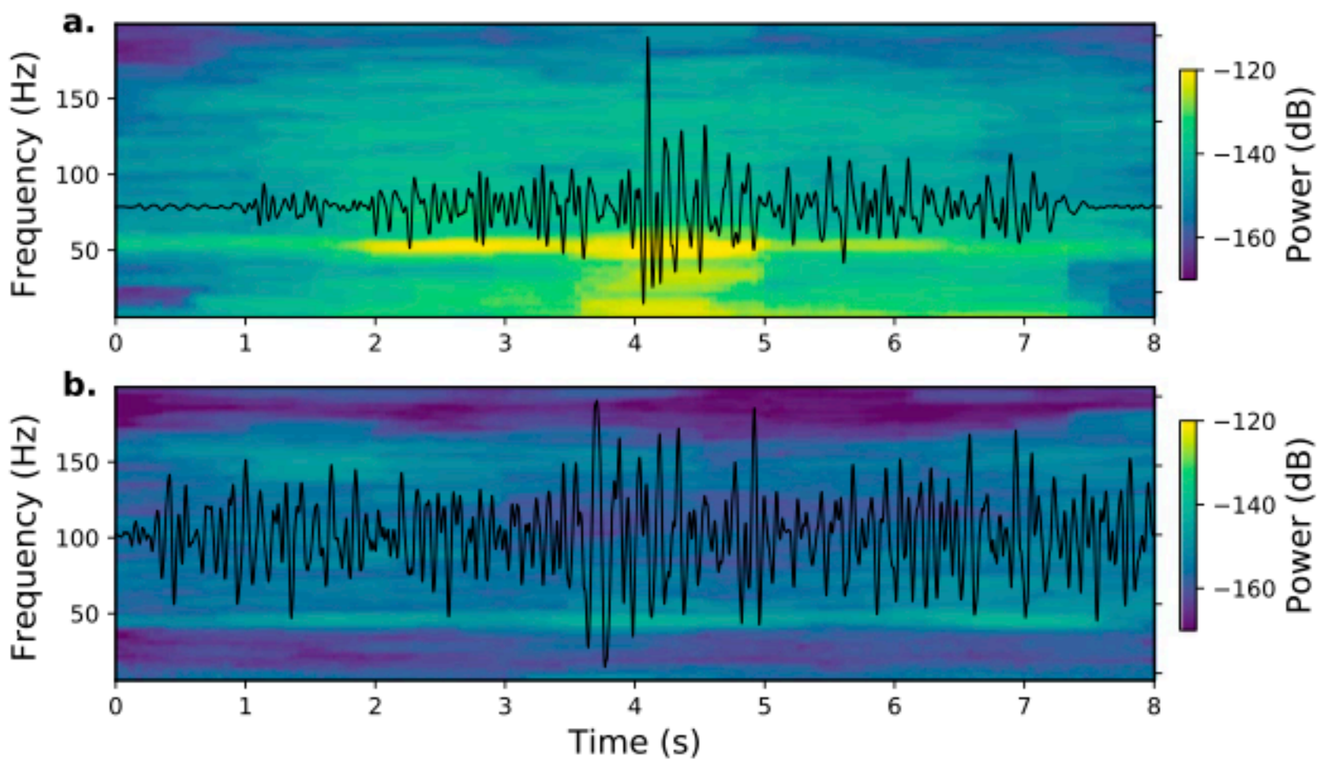

Figure 10. Earthquake-like vertical waveforms and spectrograms for 19 February 2018 11:14:48 UTC from (a) node 01-33 and (b) node 01-32 located 30 m to the west to demonstrate the variability over a short distance. Plot (a) is the same waveform shown for the vertical channel in Figure 9c.

observed in the borehole seismometer waveforms during this 1-hr period. A close-up view of the waveforms and spectrogram for a 10-min interval shows that some of these bursts in the waveforms have energy >5 Hz and amplitudes similar to the earthquake represented by the red dashed line but extending to much higher frequencies. The ground shaking seen in the spectrogram produces a diffuse increase in power lasting several minutes with an increase up to 200 Hz (Figure 11c). The low wind velocity example in Figure 11a is contrasted with a period of high wind velocity that exceeds 8 m/s at times and contains a 1-hr period of near continuous tremor-like signals (Figure 11d). The 10-min interval displayed in Figure 11e shows the sensitivity of the burst-like signals to the wind gusts (blue line). The example between 10.58 and 10.63 as the wind gusts between 5 and 7 m/s appears to produce a tremor-like burst of energy in the waveforms. The spectrogram of the 10-min interval shows increased amplitudes throughout the spectrum, with the greatest values during the tremor-like signals that have the potential to obscure naturally occurring earthquakes (Figure 11f).

Examining the horizontal waveforms for node 02-14 located 128 m north from the parking structure in the trees indicate very similar features but with reduced amplitude (Figure 12). During the nighttime hour the same signal is observed between 10.58 and 10.61 hr and the amplitude is the same order of magnitude as the earthquake shown by the red dashed line. The ground motions during the higher wind velocity show characteristics similar to node 02-11 with many bursts of high-frequency energy. The commonality between these nodes suggests that the signals are produced by numerous objects on the surface and propagate in the study area.

3.3. Nontectonic Waveforms

The data for DOY 46 and 50 are examined for transient ground motions and tectonic earthquakes using *dbpick* in the Antelope software package to manually identify nonstationary signals observed in the continuous waveforms. Exploring the waveforms by plotting all the records simultaneously and testing different filter widths highlights multiple signals originating from local structures and traversing the array. The duration of these signals varies from 2 s to hundreds of seconds. Inspection of the records for subarray 02 and 03 show earthquake-like waveforms with a radial moveout pattern originating from the foundations of structures and transient signals originating outside the study area moving across the array. An example of the radial moveout shown in Figure 13 highlights a signal originating from the parking structure. The waveforms are not filtered but normalized by the maximum amplitude of all traces to retain the relative amplitude information and the high-frequency content. When filtered between 5 and 20 Hz, the waveforms show a clear impulsive *P* wave-like signal followed by a large amplitude wave with a moveout velocity of about 450 m/s. This value is similar to the average *P* wave velocity of the subsurface material at the site

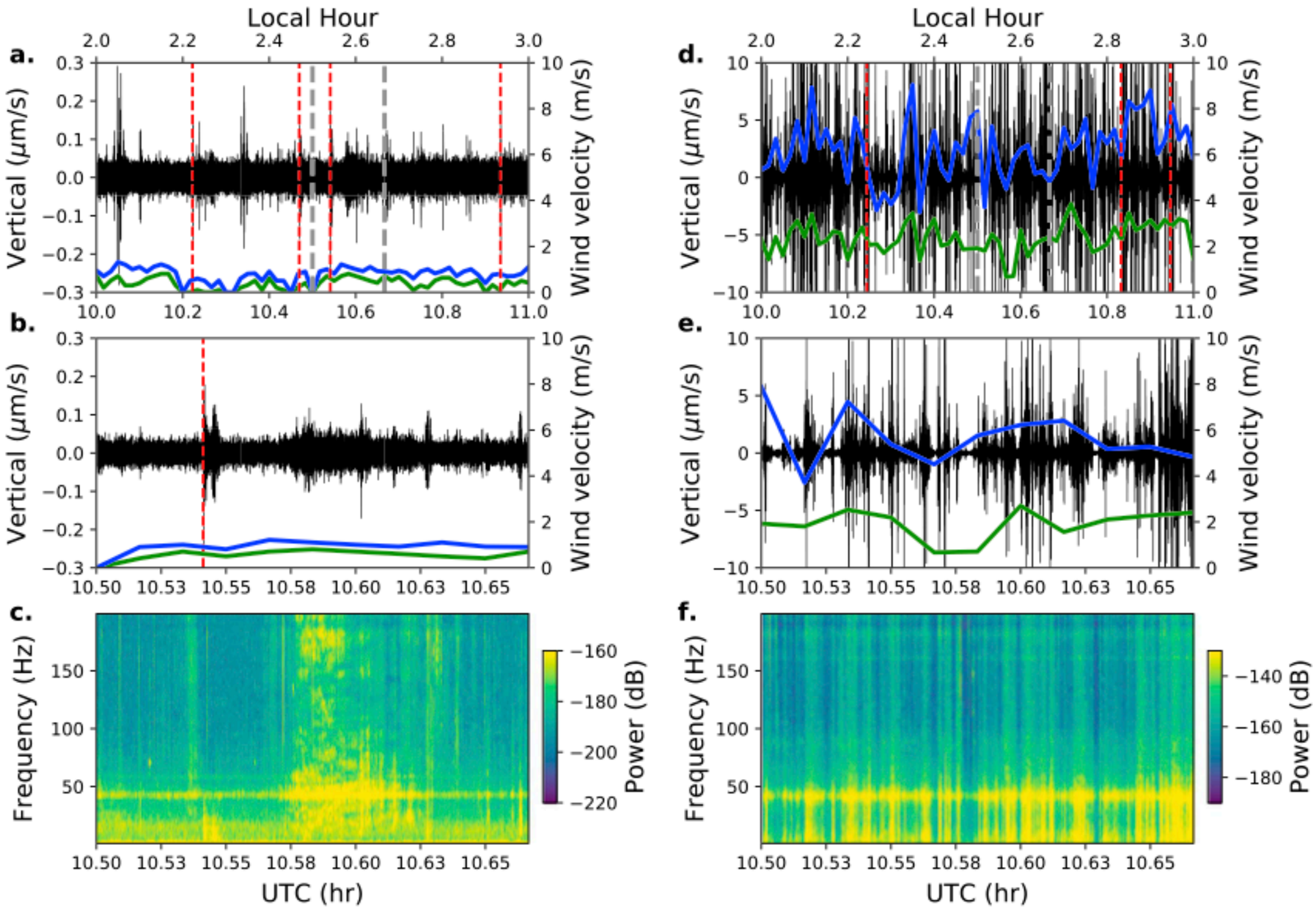

Figure 11. Earthquake- and tremor-like signals recorded on the vertical channel at node 02-11 adjacent to the parking structure during UTC 10–11 (2–3 PST) for (a–c) low wind conditions on DOY 46 and (d–f) high wind conditions on DOY 50. The average wind velocity is shown in green with peak wind velocity shown in blue. The red dashed lines are arrival times of *P* waves observed at the borehole station B946. The gray dashed lines show the 10-min interval of waveforms and spectrogram displayed in (b) and (c) and (e) and (f).

(Meng & Ben-Zion, 2018b; Mordret et al., 2019). The duration is <1 s for each signal and much shorter than the earthquake-like signals observed in the vegetation (Figures 9b and 9c).

The largest amplitude is at node 02-11 (Figure 13a), implying that the signal originates from the wind shaking the storage container adjacent to the parking structure. The signal does not attenuate as quickly as the waveform produced by the vegetation likely due to better ground coupling of the built surface structures transferring stress to the subsurface. The signal propagates ~250 m from the covered parking structure and is recorded by the 148-m-deep borehole seismometer, which shows an increase in amplitude and PSD from 5 to 15 Hz (Figure 13c). The exact source of this signal is unclear but the distance traveled, increased PSD, and clarity of this signal suggests a microfailure event in the shallow crust below the base of the structure producing a local low-amplitude seismic event (Ben-Zion et al., 2015; Hillers & Ben-Zion, 2011). Additional waveforms are observed originating from the housing structure with a moveout velocity of about 500 m/s, but the amplitude of many waveforms are an order of magnitude less than the signal observed from the example shown in Figure 13.

Not all of the observed signals originate from a local structure or vegetation within the study area as evident from moveout pattern across the subarrays. An example of a transient waveform from an unknown source beyond the study area moving across the 03 group of nodes with amplitudes that exceed an earthquake is shown in Figure 14. The transient waveforms contain high-frequency energy and indicate a source direction from the southeast. Coincidentally, a *P* wave from a local earthquake arrives immediately after the transient signal but with much lower amplitudes. The spectrogram from the borehole seismometer shows an increase in energy during the earthquake with no change detected before the *P* wave arrival during the passage of the transient waveforms (Figure 14c). If the employed nodes were installed with a spacing interval of several hundreds of meters or more, the wind-generated ground motions would be

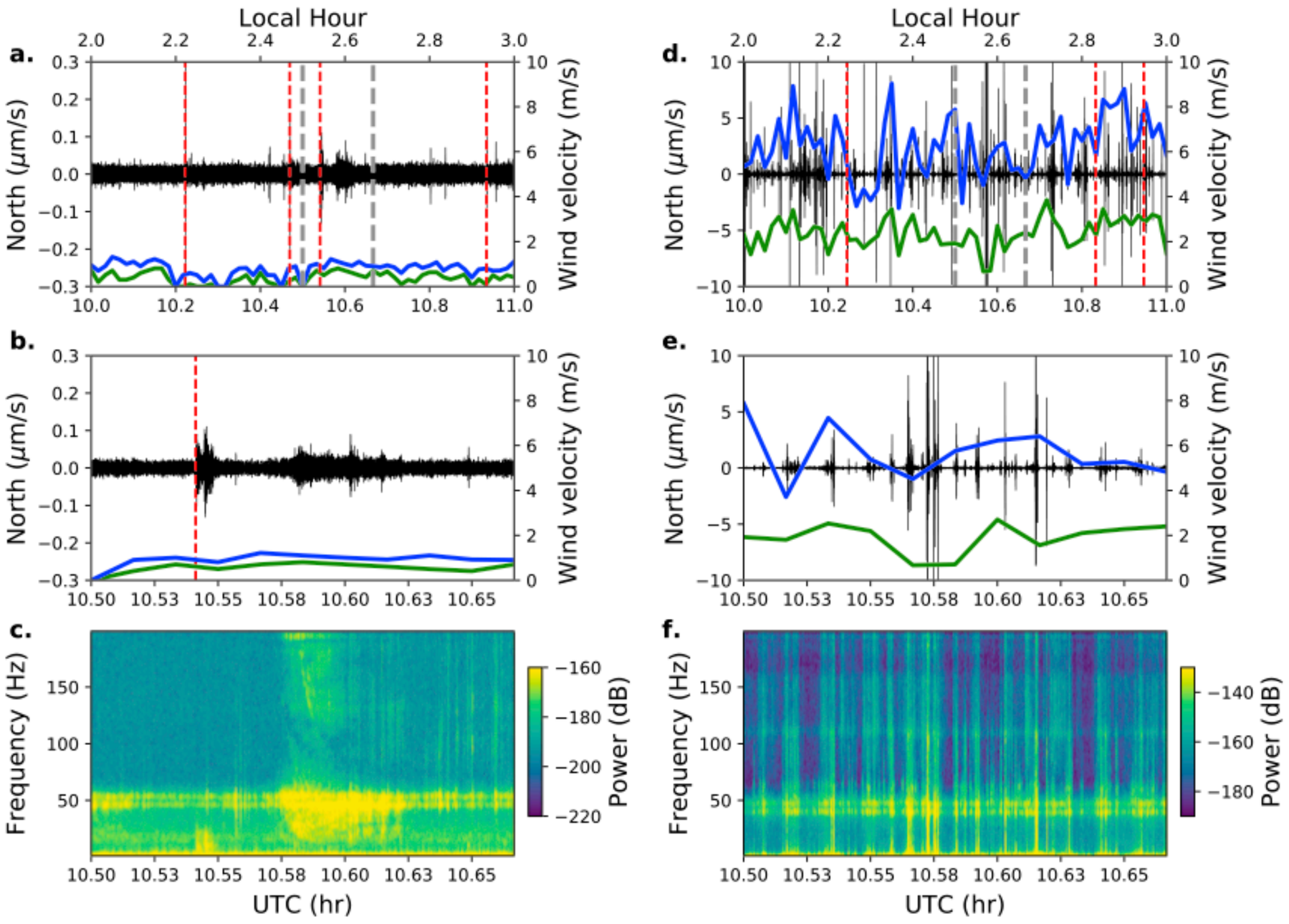

Figure 12. Earthquake- and tremor-like signals recorded on the north channel at node 02-14 located near some trees. The figure details are the same as Figure 11.

indistinguishable from tectonic events using a traditional detection algorithm based on impulsive energy and tuned for small earthquakes.

The moveout patterns for the earthquake-like waveforms are best observed using a 5–20-Hz band-pass filter, although they contain power in higher frequencies as evident in the spectrograms (e.g., Figure 11f). The filtering helps to identify the moveout pattern when all the stations are exhibiting high-frequency noise. The signals occur at all hours and are best observed during 1–2-m/s average winds. The ability to identify them decreases as the wind velocity increases, suggesting that they are present but have a low SNR and become indistinguishable from the ongoing tremor-like waveforms. On DOY 46 there are >350 waveforms traversing the 02 group of nodes. The number of detections reduces after UTC hour 17 when the sustained wind velocity is >2 m/s with wind gusts >6 m/s producing tremor-like signals. The reduced detectability of these transient signals during higher wind velocities is also apparent on DOY 50 when very few detections are made during hours of wind gusts above 6 m/s, which span 60% of the day. To assess the arrival orientations we cross correlate the waveforms for a subset of 133 transient detections that have a high enough correlation (>0.7) values to obtain the back azimuth directions (Figure 15). The data resolution prevents accurate locations beyond an arrival direction. The example shows an arrival from the northwest (Figure 15a) but we find that many of the transient signals originate from all azimuths with no preferential direction (Figure 15b). The signals containing high-frequency energy can have multiple origins, including various induced local subsurface failures, and require additional detailed study with multiscale array over a larger region to fully characterize the signals.

4. Discussion

The data indicate that 6–31% of the day at the SGB study area have wind-generated ground motions with high-frequency content and long durations that can mask detection of microseismic earthquakes and tectonic tremor. During wind gusts of velocities >3 m/s, earthquake- and tremor-like signals originate from

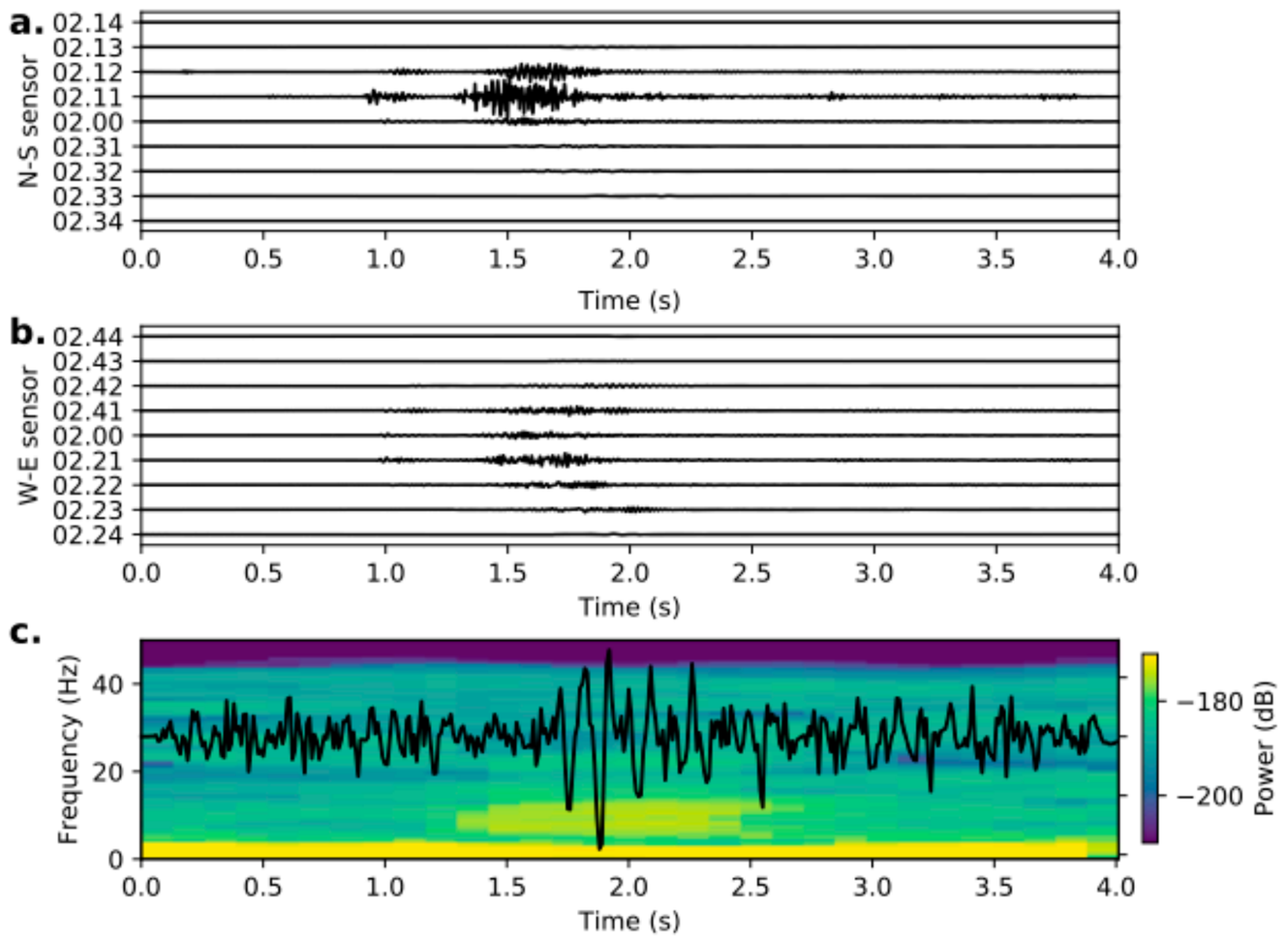

Figure 13. Earthquake-like ground motions produced from local structures and observations of signals propagating to nearby borehole seismometer at 15 February 2018 14:54:00 UTC. The unfiltered nodal waveforms show ground shaking originating from the covered parking structure. The (a) north-south transect and the (b) east-west transect both show a radial pattern originating from the structure. (c) The borehole seismometer waveforms and spectrogram indicate an arrival consistent in time for this event, but others in the data are not always observed at depth.

the trees, bushes, and built structures and produce ongoing energy and possible microfailures in the shallow crust that elevate the local noise (Ben-Zion et al., 2015; Hillers & Ben-Zion, 2011; Johnson et al., 2019). The high frequencies and rapid attenuation of these signals suggest that the wind interaction with surface objects lead to wave energy in the shallow crust that is modified considerably during propagation (Withers et al., 1996). The examples presented are representative of earthquake- and tremor-like wind-related waveforms for the SGB site and should not be considered templates for this class of signals. In general, the wind-related waveforms are expected to vary strongly depending on site conditions at and around the node location as well as spatial distribution of obstacles above the ground (Figure 3). The process is not unique to the subset of data presented and is expected to occur with variations essentially in all environments. Nontectonic signals should be classified properly to reduce false detections of small earthquakes and tectonic tremor, quantifying seasonal or long-term trends in the continuous recordings, and imaging the subsurface with ambient noise.

High-frequency seismic signals are of particular interest to characterize source properties of microseismic events (Kwiatek & Ben-Zion, 2016) and image the upper 500 m of the crust (Hillers et al., 2016; Mordret et al., 2019; Roux et al., 2016; Zigone et al., 2019). The presented data contain high-frequency nontectonic signals up to 200 Hz that are near continuous for many hours during elevated wind conditions, and not expected to originate from a single source location as shown by the variation in amplitude throughout the study area (Figure 3). The noise amplification decays with distance with respect to the proximity to obstacles above the surface which indicates some objects act as sources of high-frequency energy (Figure 6). However, the ubiquity of these signals at all nodes with a quantifiable variation at different wind velocities suggests that multiple processes are contributing the noise signals.

Possible contributions to these high-frequency signals include direct wind coupling to the surface mounted recording instruments (Withers et al., 1996) and turbulent and shear stresses from wind interaction with the ground (Naderyan et al., 2016; Raspet et al., 2008; Yu et al., 2011). Withers et al. (1996) found that surface seismic noise is present up to 60 Hz during winds above 3 m/s and is reduced when installing seismometers at a depth of 43 m, but still present at frequencies less than 20–30 Hz. The results from the 148-m borehole station show correlated noise with winds above 2 m/s and indicate attenuation of the high-frequency noise with signals present at less than 8 Hz (Figure 7). Naderyan et al. (2016) modeled the predicted power

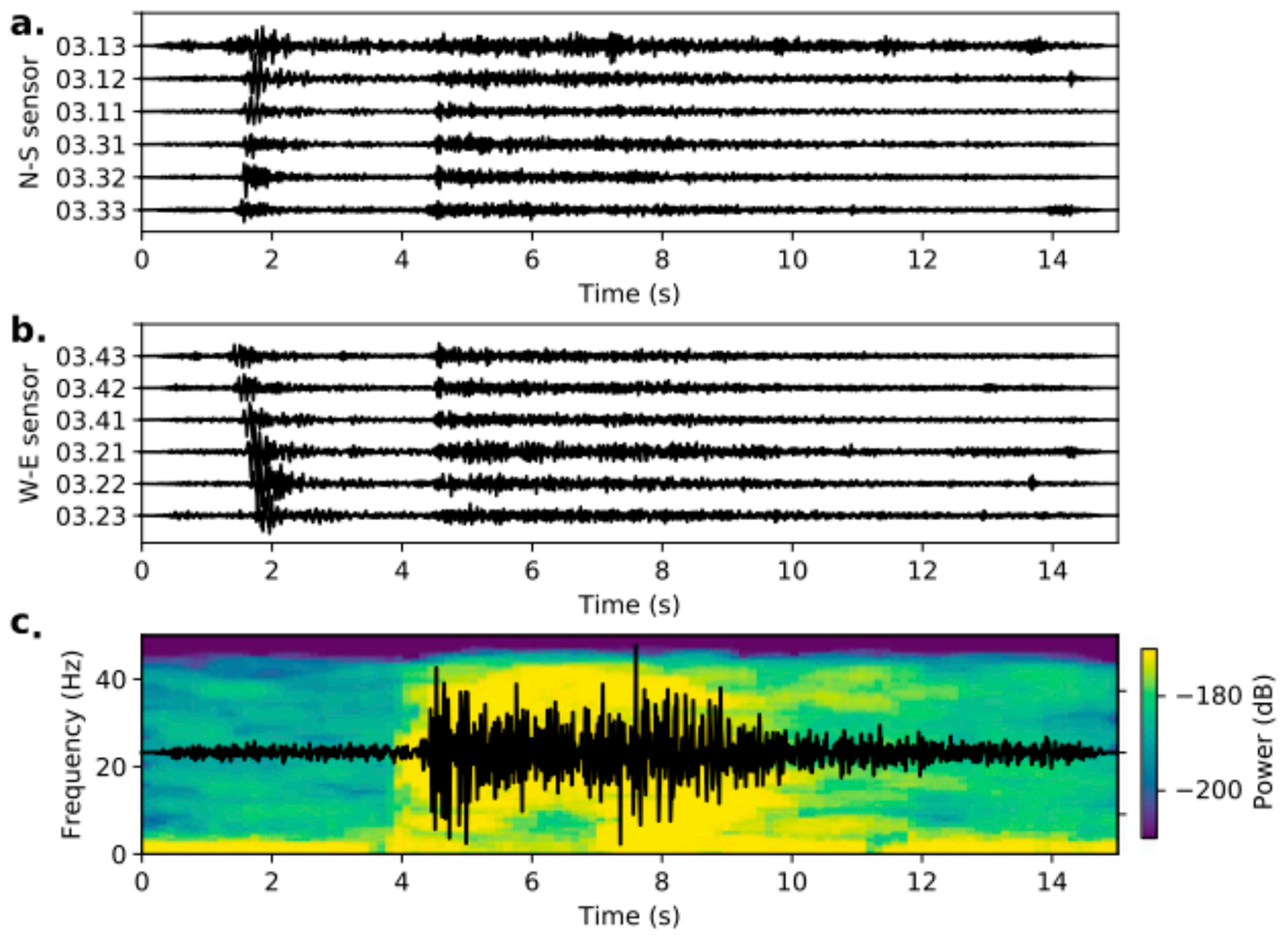

Figure 14. (a and b) Transient ground motions moving across the 03 group of nodes with larger amplitudes than the earthquake arrival around 5 s on 15 February 2018 01:14:00 UTC. (c) Waveform and spectrogram from the borehole seismometer showing the temporal and spectral features of an earthquake without any indication of the passage of the transient signal.

spectrum for horizontal and vertical ground motions from wind turbulence and found good agreement in the vertical component data, but significantly underpredicts the horizontal ground motions regardless of burial depth. The lack of depth dependence and correlation with wind velocity demonstrate that the source is not direct wind interactions with the instrument and possibly originating from a nearby fence coupling wind energy into the ground. A plausible explanation of the high-frequency noise and horizontal ground motions is that the forces produced by the wind at the base of trees, vegetation, and structures deform the subsurface and lead to local failures. In shallow materials with low overburden pressure, deformation is essentially controlled by the effective cohesion with values between 5 and 50 kPa that vary with matric suction due to pore pressure changes (Dupuy et al., 2007; Rahardjo et al., 2009). Laboratory experiments indicate that geomaterials under low confining pressure fail under strain levels as low as 10^{-7} (e.g., Pasqualini et al., 2007; TenCate et al., 2004). Such strain levels are likely to be produced around the bases of trees and structures deflected by the wind, leading to micro brittle failures involving transient changes of elastic moduli and generation of high-frequency radiation (Ben-Zion & Ampuero, 2009). Detailed understanding of the observed high-frequency waves requires more detailed observations and modeling that are beyond the scope of the present study.

Improved detection of microseismic events requires identification of first arrivals with a SNR close to 1, and the ability to separate genuine events from similar signals originating from nontectonic sources. Impulsive signals with a high SNR are recognizable by algorithms searching for a change in waveform energy (Withers et al., 1998), but are not sophisticated enough to discern nontectonic signals with the same characteristics. Waveform similarity techniques such as match-filter (Gibbons & Ringdal, 2006) or subspace singular value decomposition (Harris, 2006) can identify signals with low SNR but require predefined example waveforms and parametric thresholds that could result in false detections from earthquake-like waveforms such as those documented in this paper (e.g., Figure 9). The spatial and temporal variabilities of waveforms at the SGB site (e.g., Figure 10) demonstrate that more advanced detection techniques are needed to identify multiple classes of waveforms originating from diverse sources with spectral and temporal features similar to earthquakes.

Machine learning algorithms have shown positive results for discriminating earthquakes from rockslides, quarry blasts, and avalanches (Glasgow et al., 2018; Hammer et al., 2013; Kuyuk et al., 2011; Rubin et al., 2012), and are being tested to enhance earthquake detection using regional networks (Aguiar & Beroza,

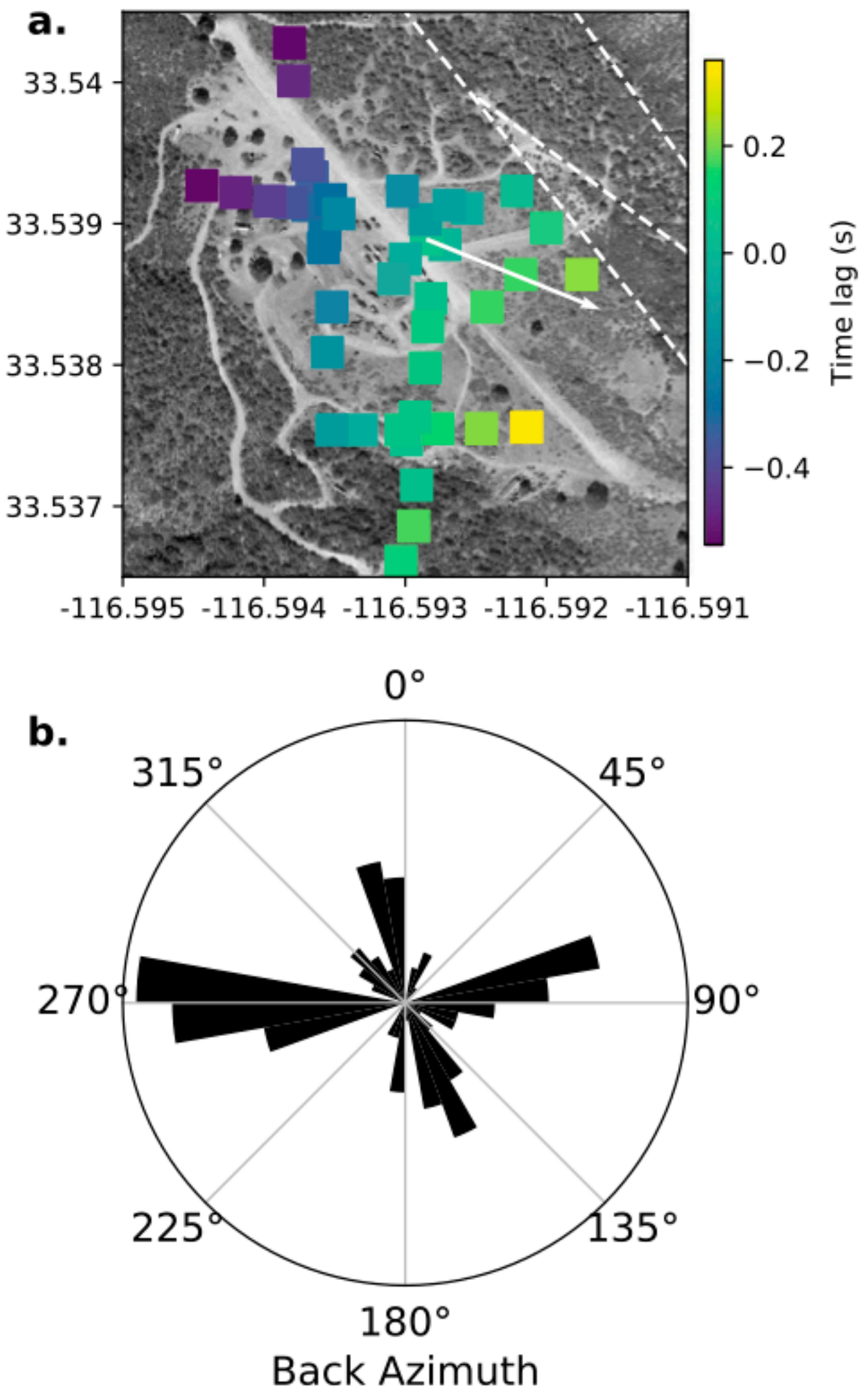

Figure 15. Back azimuth obtained from cross-correlation time lag of transient signals. (a) Example time lag of signal traversing the array with a back azimuth of 113° shown by the white arrow. Squares indicate the node location and are colored by the time lag. (b) Polar histogram of the back azimuth determined for 133 transient events on two days of the deployment.

2014; Barrett & Beroza, 2014; Hammer et al., 2012; Perol et al., 2018; Reynen & Audet, 2017; Ruano et al., 2014; Yoon et al., 2015). Such techniques with time- and frequency-domain data features to target varying noise signals can help evaluate the detections and reduce the rate of false positives. In particular, implementing supervised learning techniques using engineered features derived from earthquake physics and signal processing metrics may provide new insight about the physical process of earthquakes and other tectonic signals. Our results demonstrate that blind implementation of a detection algorithm can identify earthquake-like waveforms that are not originating from tectonic sources and result in false-positive detections that require removal during an association algorithm to locate.

There is considerable interest in the detection of tremor that represents a bridge between seismic and aseismic motions (e.g., Ide et al., 2008; Peng & Gomberg, 2010). The results of this study show emergent tremor-like signals that are produced by atmospheric processes coupling to the ground. Airplanes and helicopters can also produce tremor-like signals (Eibl et al., 2015; Meng & Ben-Zion, 2018a). Some studies inferred the existence of tectonic tremor in the SJFZ (Hutchison & Ghosh, 2017; Wang et al., 2013), but these observations may have been produced by anthropogenic sources in the frequency band consistent with tremor observations (Inbal et al., 2018). We expect tremor detectability to be reduced by wind-related ground

motion (e.g., Figures 3 and 7) further than the thresholds discussed for small earthquakes due to the emergent low-amplitude nature of tremor. The air-traffic signals documented by Meng and Ben-Zion (2018a) that occupy >7% of the daily recording at the SGB site are similar to the wind generated tremor-like signals presented in Figure 9 but with durations of hundreds of seconds. The spectrograms of air-traffic events include clear Doppler effects indicating a moving acoustic source, but otherwise contain similar spectral features as the wind-generated ground motions. We emphasize again that details of the spectral content and waveform characteristics of the wind-related events depend on local propagation and attenuation properties of the subsurface, so they may appear differently at other locations. The results demonstrate the need to carefully evaluate earthquake- and tremor-like signals observed in dense array and regional network data.

5. Conclusions

Wind-related ground motions produce a class of waveforms that occupy a significant percentage of continuous seismic records and affect sensors both at the surface and shallow boreholes. As dense deployments become more common in the scientific community, the need to properly classify signals becomes more important to reduce false detection of tectonic events. In the SGB study area, about 6–31% of the day has wind conditions that produce PGV greater than the ground motions expected from local M1.0–1.5 earthquakes, thereby limiting the ability to detect such and smaller microseismic events. Tremor-like signals generated by high wind conditions are expected to occur in many regions and caution should be exercised to separate such events from tectonic tremor in data of dense arrays and regional seismic networks.

Acknowledgments
We thank Nori Nakata for providing the sensors used to record the data analyzed in this study. The data can be obtained from the Data Management Center of the Incorporated Research Institutions for Seismology and Broadband Seismic Data Collection doi.org/10.7914/SN/7A_2018 (Johnson et al., 2018). C.W.J. is funded by the National Science Foundation EAR Postdoctoral Fellowship award 1725344. The study was supported by the Southern California Earthquake Center (based on NSF cooperative agreement EAR-1600087 and USGS cooperative agreement G17AC00047) and the National Science Foundation (grant EAR-1818589). No authors have any real or perceived financial conflicts of interests. The paper benefited from useful comments by two anonymous referees and an anonymous Associate Editor.

References

Aguiar, A. C., & Beroza, G. C. (2014). PageRank for earthquakes. *Seismological Research Letters*, *85*(2), 344–350. https://doi.org/10.1785/0220130162

Aster, R. C., & Shearer, P. M. (1991). High-frequency borehole seismograms recorded in the San Jcinto Fault zone, Southern California: Part 2—Attenuation and site effects. *Bulletin of the Seismological Society of America*, *81*(4), 1081–1100.

Barrett, S. A., & Beroza, G. C. (2014). An empirical approach to subspace detection. *Seismological Research Letters*, *85*(3), 594–600. https://doi.org/10.1785/0220130152

Bensen, G. D., Ritzwoller, M. H., Barmin, M. P., Levshin, A. L., Lin, F., Moschetti, M. P., et al. (2007). Processing seismic ambient noise data to obtain reliable broad-band surface wave dispersion measurements. *Geophysical Journal International*, *169*(3), 1239–1260. https://doi.org/10.1111/j.1365-246X.2007.03374.x

Ben-Zion, Y., & Ampuero, J.-P. (2009). Seismic radiation from regions sustaining material damage. *Geophysical Journal International*, *178*(3), 1351–1356. https://doi.org/10.1111/j.1365-246X.2009.04285.x

Ben-Zion, Y., Vernon, F. L., Ozakin, Y., Zigone, D., Ross, Z. E., Meng, H., et al. (2015). Basic data features and results from a spatially dense seismic array on the San Jacinto fault zone. *Geophysical Journal International*, *202*(1), 370–380. https://doi.org/10.1093/gji/ggv142

Bonilla, L. F. N., Steidl, J. H., Gariel, J.-C., & Archuleta, R. J. (2002). Borehole response studies at the Garner Valley Downhole Array, Southern California. *Bulletin of the Seismological Society of America*, *92*(8), 3165–3179. https://doi.org/10.1785/0120010235

Campillo, M., Roux, P., & Shapiro, N. M. (2011). Seismic, Ambient Noise Correlation. In H. K. Gupta (Ed.), *Encyclopedia of Solid Earth Geophysics* (pp. 1230–1236). Dordrecht, Netherlands: Springer. https://doi.org/10.1007/978-90-481-8702-7_218

Corciulo, M., Roux, P., Campillo, M., Dubucq, D., & Kuperman, W. A. (2012). Multiscale matched-field processing for noise-source localization in exploration geophysics. *Geophysics*, *77*(5), KS33–KS41. https://doi.org/10.1190/geo2011-0438.1

De Angelis, S., & Bodin, P. (2012). Watching the wind: Seismic data contamination at long periods due to atmospheric pressure-field-induced tilting. *Bulletin of the Seismological Society of America*, *102*(3), 1255–1265. https://doi.org/10.1785/0120110186

Dupuy, L. X., Fourcaud, T., Lac, P., & Stokes, A. (2007). A generic 3D Finite element model of tree anchorage integrating soil mechanics and real root system architecture. *American Journal of Botany*, *94*(9), 1506–1514. https://doi.org/10.3732/ajb.94.9.1506

Dybing, S. N., Ringler, A. T., Wilson, D. C., & Anthony, R. E. (2019). Characteristics and spatial variability of wind noise on near-surface broadband seismometerscharacteristics and spatial variability of wind noise on near-surface broadband seismometers. *Bulletin of the Seismological Society of America.*, *109*(3), 1082–1098. https://doi.org/10.1785/0120180227

Eibl, E. P. S., Lokmer, I., Bean, C. J., Akerlie, E., & Vogfjörd, K. S. (2015). Helicopter vs. volcanic tremor: Characteristic features of seismic harmonic tremor on volcanoes. *Journal of Volcanology and Geothermal Research*, *304*, 108–117. https://doi.org/10.1016/j.jvolgeores.2015.08.002

Farrell, J., Wu, S. M., Ward, K. M., & Lin, F. C. (2018). Persistent noise signal in the Fairfield nodal three-component 5-Hz geophones. *Seismological Research Letters*, *89*(5), 1609–1617. https://doi.org/10.1785/0220180073

Gibbons, S. J., & Ringdal, F. (2006). The detection of low magnitude seismic events using array-based waveform correlation. *Geophysical Journal International*, *165*(1), 149–166. https://doi.org/10.1111/j.1365-246X.2006.02865.x

Glasgow, M. E., Schmandt, B., & Hansen, S. M. (2018). Upper crustal low-frequency seismicity at Mount St. Helens detected with a dense geophone array. *Journal of Volcanology and Geothermal Research*, *358*, 329–341. https://doi.org/10.1016/j.jvolgeores.2018.06.006

Gradon, C., Moreau, L., Roux, P., & Ben-Zion, Y. (2019). Analysis of surface and seismic sources in dense array data with match field processing and Markov chain Monte Carlo sampling. *Geophysical Journal International.*, *218*(2), 1044–1056. https://doi.org/10.1093/gji/ggz224

Hammer, C., Beyreuther, M., & Ohrnberger, M. (2012). A seismic-event spotting system for volcano fast-response systems. *Bulletin of the Seismological Society of America*, *102*(3), 948–960. https://doi.org/10.1785/0120110167

Hammer, C., Ohrnberger, M., & Fäh, D. (2013). Classifying seismic waveforms from scratch: A case study in the alpine environment. *Geophysical Journal International*, *192*(1), 425–439. https://doi.org/10.1093/gji/ggs036

Harris, D. B. (2006). *Subspace detectors: Theory*. United States: Department of Energy.
Hillers, G., & Ben-Zion, Y. (2011). Seasonal variations of observed noise amplitudes at 2–18 Hz in Southern California. *Geophysical Journal International*, *184*(2), 860–868. https://doi.org/10.1111/j.1365-246X.2010.04886.x
Hillers, G., Roux, P., Campillo, M., & Ben-Zion, Y. (2016). Focal spot imaging based on zero lag cross-correlation amplitude fields: Application to dense array data at the San Jacinto fault zone. *Journal of Geophysical Research: Solid Earth*, *121*, 8048–8067. https://doi.org/10.1002/2016JB013014
Hutchison, A. A., & Ghosh, A. (2017). Ambient tectonic tremor in the San Jacinto Fault, near the Anza Gap, Detected by multiple mini seismic arrays ambient tectonic tremor in the San Jacinto Fault, near the Anza Gap, detected by multiple mini seismic arrays. *Bulletin of the Seismological Society of America*, *107*(5), 1985–1993. https://doi.org/10.1785/0120160385
Ide, S., Imanishi, K., Yoshida, Y., Beroza, G. C., & Shelly, D. R. (2008). Bridging the gap between seismically and geodetically detected slow earthquakes. *Geophysical Research Letters*, *35*, L10305. https://doi.org/10.1029/2008GL034014
Inbal, A., Cristea-Platon, T., Ampuero, J. P., Hillers, G., Agnew, D., & Hough, S. E. (2018). Sources of long-range anthropogenic noise in Southern California and implications for tectonic tremor detection. *Bulletin of the Seismological Society of America*, *108*(6), 3511–3527. https://doi.org/10.1785/0120180130
Johnson, C. W., Vernon, F., Ben-Zion, Y., & Nakata, N. (2018). Sage Brush Flats seismic experiment on interaction of wind with ground motion. Retrieved from: https://doi.org/10.7914/SN/7A_2018
Johnson, C. W., Vernon, F., Nakata, N., & Ben-Zion, Y. (2019). Atmospheric processes modulating noise in Fairfield nodal 5 Hz geophones. *Seismological Research Letters*. https://doi.org/10.1785/0220180383
Kuperman, W. A., & Turek, G. (1997). Matched field acoustics. *Mechanical Systems and Signal Processing*, *11*(1), 141–148. https://doi.org/10.1006/mssp.1996.0066
Kurzon, I., Vernon, F. L., Ben-Zion, Y., & Atkinson, G. (2014). Ground motion prediction equations in the San Jacinto Fault Zone: Significant effects of rupture directivity and fault zone amplification. *Pure and Applied Geophysics*, *171*(11), 3045–3081. https://doi.org/10.1007/s00024-014-0855-2
Kuyuk, H., Yildirim, E., Dogan, E., & Horasan, G. (2011). An unsupervised learning algorithm: Application to the discrimination of seismic events and quarry blasts in the vicinity of Istanbul. *Natural Hazards and Earth System Sciences*, *11*(1), 93–100. https://doi.org/10.5194/nhess-11-93-2011
Kwiatek, G., & Ben-Zion, Y. (2016). Theoretical limits on detection and analysis of small earthquakes. *Journal of Geophysical Research: Solid Earth*, *121*, 5898–5916. https://doi.org/10.1002/2016JB012908
Liu, X., & Ben-Zion, Y. (2016). Estimating correlations of neighbouring frequencies in ambient seismic noise. *Geophysical Journal International*, *206*(2), 1065–1075. https://doi.org/10.1093/gji/ggw196
Liu, X., Ben-Zion, Y., & Zigone, D. (2015). Extracting seismic attenuation coefficients from cross-correlations of ambient noise at linear triplets of stations. *Geophysical Journal International*, *203*(2), 1149–1163. https://doi.org/10.1093/gji/ggv357
Lobkis, O. I., & Weaver, R. L. (2001). On the emergence of the Green's function in the correlations of a diffuse field. *The Journal of the Acoustical Society of America*, *110*(6), 3011–3017. https://doi.org/10.1121/1.1417528
Lott, F. F., Ritter, J. R. R., Al-Qaryouti, M., & Corsmeier, U. (2017). On the analysis of wind-induced noise in seismological recordings. *Pure and Applied Geophysics*, *174*(3), 1453–1470. https://doi.org/10.1007/s00024-017-1477-2
Marcillo, O. E., & Carmichael, J. (2018). The detection of wind-turbine noise in seismic records. *Seismological Research Letters*, *89*(5), 1826–1837. https://doi.org/10.1785/0220170271
Meng, H., & Ben-Zion, Y. (2018a). Characteristics of airplanes and helicopters recorded by a dense seismic array near Anza California. *Journal of Geophysical Research: Solid Earth*, *123*, 4783–4797. https://doi.org/10.1029/2017JB015240
Meng, H., & Ben-Zion, Y. (2018b). Detection of small earthquakes with dense array data: Example from the San Jacinto fault zone, Southern California. *Geophysical Journal International*, *212*(1), 442–457. https://doi.org/10.1093/gji/ggx404
Mordret, A., Roux, P., Boué, P., & Ben-Zion, Y. (2019). Shallow three-dimensional structure of the San Jacinto fault zone revealed from ambient noise imaging with a dense seismic array. *Geophysical Journal International*, *216*(2), 896–905. https://doi.org/10.1093/gji/ggy464
Mucciarelli, M., Gallipoli, M. R., Di Giacomo, D., Di Nota, F., & Nino, E. (2005). The influence of wind on measurements of seismic noise. *Geophysical Journal International*, *161*(2), 303–308. https://doi.org/10.1111/j.1365-246X.2004.02561.x
Naderyan, V., Hickey, C. J., & Raspet, R. (2016). Wind-induced ground motion. *Journal of Geophysical Research: Solid Earth*, *121*, 917–930. https://doi.org/10.1002/2015JB012478
Pasqualini, D., Heitmann, K., TenCate, J. A., Habib, S., Higdon, D., & Johnson, P. A. (2007). Nonequilibrium and nonlinear dynamics in Berea and Fontainebleau sandstones: Low-strain regime. *Journal of Geophysical Research*, *112*, B01204. https://doi.org/10.1029/2006JB004264
Peng, Z., & Gomberg, J. (2010). An integrated perspective of the continuum between earthquakes and slow-slip phenomena. *Nature Geoscience*, *3*(9), 599–607. https://doi.org/10.1038/ngeo940
Perol, T., Gharbi, M., & Denolle, M. (2018). Convolutional neural network for earthquake detection and location. *Science Advances*, *4*(2), e1700578. https://doi.org/10.1126/sciadv.1700578
Prieto, G. A., Parker, R. L., & Vernon, F. L. (2009). A Fortran 90 library for multitaper spectrum analysis. *Computers & Geosciences*, *35*(8), 1701–1710. https://doi.org/10.1016/j.cageo.2008.06.007
Rahardjo, H., Harnas, F. R., Leong, E. C., Tan, P. Y., Fong, Y. K., & Sim, E. K. (2009). Tree stability in an improved soil to withstand wind loading. *Urban Forestry & Urban Greening*, *8*(4), 237–247. https://doi.org/10.1016/j.ufug.2009.07.001
Raspet, R., Yu, J., & Webster, J. (2008). Low frequency wind noise contributions in measurement microphones. *The Journal of the Acoustical Society of America*, *123*(3), 1260–1269. https://doi.org/10.1121/1.2832329
Reynen, A., & Audet, P. (2017). Supervised machine learning on a network scale: Application to seismic event classification and detection. *Geophysical Journal International*, *210*(3), 1394–1409. https://doi.org/10.1093/gji/ggx238
Riahi, N., & Gerstoft, P. (2015). The seismic traffic footprint: Tracking trains, aircraft, and cars seismically. *Geophysical Research Letters*, *42*, 2674–2681. https://doi.org/10.1002/2015GL063558
Ross, Z. E., Hauksson, E., & Ben-Zion, Y. (2017). Abundant off-fault seismicity and orthogonal structures in the San Jacinto fault zone. *Science Advances*, *3*(3), e1601946. https://doi.org/10.1126/sciadv.1601946
Ross, Z. E., Meier, M.-A., & Hauksson, E. (2018). *P* wave arrival picking and first-motion polarity determination with deep learning. *Journal of Geophysical Research: Solid Earth*, *123*, 5120–5129. https://doi.org/10.1029/2017JB015251
Roux, P., Moreau, L., Lecointre, A., Hillers, G., Campillo, M., Ben-Zion, Y., et al. (2016). A methodological approach towards high-resolution surface wave imaging of the San Jacinto Fault Zone using ambient-noise recordings at a spatially dense array. *Geophysical Journal International*, *206*(2), 980–992. https://doi.org/10.1093/gji/ggw193

Ruano, A. E., Madureira, G., Barros, O., Khosravani, H. R., Ruano, M. G., & Ferreira, P. M. (2014). Seismic detection using support vector machines. *Neurocomputing*, *135*, 273–283. https://doi.org/10.1016/j.neucom.2013.12.020

Rubin, M. J., Camp, T., Herwijnen, A. V., & Schweizer, J. (2012, 12-15 Dec. 2012). Automatically detecting avalanche events in passive seismic data. Paper presented at the 2012 11th International Conference on Machine Learning and Applications.

Sánchez-Sesma, F. J., Pérez-Ruiz, J. A., Luzón, F., Campillo, M., & Rodríguez-Castellanos, A. (2008). Diffuse fields in dynamic elasticity. *Wave Motion*, *45*(5), 641–654. https://doi.org/10.1016/j.wavemoti.2007.07.005

Schmandt, B., & Clayton, R. W. (2013). Analysis of teleseismic *P* waves with a 5200-station array in Long Beach, California: Evidence for an abrupt boundary to Inner Borderland rifting. *Journal of Geophysical Research: Solid Earth*, *118*, 5320–5338. https://doi.org/10.1002/jgrb.50370

Shelly, D. R., Hardebeck, J. L., Ellsworth, W. L., & Hill, D. P. (2016). A new strategy for earthquake focal mechanisms using waveform-correlation-derived relative polarities and cluster analysis: Application to the 2014 Long Valley Caldera earthquake swarm. *Journal of Geophysical Research: Solid Earth*, *121*, 8622–8641. https://doi.org/10.1002/2016JB013437

Sorrells, G. G. (1971). Preliminary investigation into relationship between long-period seismic noise and local fluctuations in atmospheric-pressure field. *Geophysical Journal of the Royal Astronomical Society*, *26*(1–4), 71–82. https://doi.org/10.1111/j.1365-246X.1971.tb03383.x

Sorrells, G. G., & Goforth, T. T. (1973). Low-frequency Earth motion generated by slowly propagating partially organized pressure fields. *Bulletin of the Seismological Society of America*, *63*(5), 1583–1601.

Sorrells, G. G., McDonald, J. A., Herrin, E., & Der, Z. A. (1971). Earth motion caused by local atmospheric-pressure changes. *Geophysical Journal of the Royal Astronomical Society*, *26*(1–4), 83–98. https://doi.org/10.1111/j.1365-246X.1971.tb03384.x

Sweet, J. R., Anderson, K. R., Bilek, S., Brudzinski, M., Chen, X., DeShon, H., et al. (2018). A community experiment to record the full seismic wavefield in Oklahoma. *Seismological Research Letters*, *89*(5), 1923–1930. https://doi.org/10.1785/0220180079

Tanimoto, T., & Valovcin, A. (2016). Existence of the threshold pressure for seismic excitation by atmospheric disturbances. *Geophysical Research Letters*, *43*, 11,202–211,208. https://doi.org/10.1002/2016GL070858

Tanimoto, T., & Wang, J. (2018). Low-frequency seismic noise characteristics from the analysis of co-located seismic and pressure data. *Journal of Geophysical Research: Solid Earth*, *123*, 5853–5885. https://doi.org/10.1029/2018JB015519

TenCate, J. A., Pasqualini, D., Habib, S., Heitmann, K., Higdon, D., & Johnson, P. A. (2004). Nonlinear and nonequilibrium dynamics in geomaterials. *Physical Review Letters*, *93*(6), 065501. https://doi.org/10.1103/PhysRevLett.93.065501

Thomson, D. J. (1982). Spectrum estimation and harmonic analysis. *Proceedings of the IEEE*, *70*(9), 1055–1096. https://doi.org/10.1109/PROC.1982.12433

Wang, T. H., Cochran, E. S., Agnew, D., & Oglesby, D. D. (2013). Infrequent triggering of tremor along the San Jacinto Fault near Anza, California. *Bulletin of the Seismological Society of America*, *103*(4), 2482–2497. https://doi.org/10.1785/0120120284

Weaver, R. L. (1982). On diffuse waves in solid media. *The Journal of the Acoustical Society of America*, *71*(6), 1608–1609. https://doi.org/10.1121/1.387816

Withers, M., Aster, R., Young, C., Beiriger, J., Harris, M., Moore, S., & Trujillo, J. (1998). A comparisoin of select trigger algorithms for automated global seismic phase and event detection. *Bulletin of the Seismological Society of America*, *88*(1), 95–106.

Withers, M. M., Aster, R. C., Young, C. J., & Chael, E. P. (1996). High-frequency analysis of seismic background noise as a function of wind speed and shallow depth. *Bulletin of the Seismological Society of America*, *86*(5), 1507–1515.

Yoon, C. E., O'Reilly, O., Bergen, K. J., & Beroza, G. C. (2015). Earthquake detection through computationally efficient similarity search. *Science Advances*, *1*(11). https://doi.org/10.1126/sciadv.1501057

Yu, J., Raspet, R., Webster, J., & Abbott, J. (2011). Wind noise measured at the ground surface. *The Journal of the Acoustical Society of America*, *129*(2), 622–632. https://doi.org/10.1121/1.3531809

Zigone, D., Ben-Zion, Y., Lehujeur, M., Campillo, M., Hillers, G., & Vernon, F. L. (2019). Imaging subsurface structures in the San Jacinto fault zone with high-frequency noise recorded by dense linear arrays. *Geophysical Journal International*, *217*(2), 879–893. https://doi.org/10.1093/gji/ggz069